Advances in solution-processed near-infrared light-emitting diodes

Maria Vasilopoulou[1,∫,*], Azhar Fakharuddin[2,∫], F. Pelayo García de Arquer[3,4], Dimitra G. Georgiadou[5,6], Hobeom Kim[7], Abd. Rashid bin Mohd Yusoff[8], Feng Gao[9], Mohammad Khaja Nazeeruddin[7], Henk J. Bolink[10,*], Edward H. Sargent[3,*]

[1]Institute of Nanoscience and Nanotechnology, National Center for Scientific Research Demokritos, 15341 Agia Paraskevi, Attica, Greece

[2]Department of Physics, University of Konstanz, 78464 Konstanz, Germany

[3]Department of Electrical and Computer Engineering, University of Toronto, Toronto, ON, M5S 3G4, Canada

[4]ICFO - Institut de Ciències Fotòniques, The Barcelona Institute of Science and Technology, Barcelona 08860, Spain

[4]Zepler Institute for Photonics and Nanoelectronics, University of Southampton, SO17 1BJ Southampton, United Kingdom

[5]Department of Physics, Imperial College London, SW7 2AZ London, United Kingdom

[6]Institute of Chemical Sciences and Engineering, École Polytechnique Fédérale de Lausanne (EPFL), Rue de l'Industrie 17, CH-1951 Sion, Switzerland

[7]Department of Chemical Engineering, Pohang University of Science and Technology (POSTECH), Pohang, Gyeongbuk 37673, Republic of Korea

[8]Department of Physics, Chemistry and Biology (IFM), Linköping University, Sweden

[9]Instituto de Ciencia Molecular, Universidad de Valencia, Calle Catedrático Jose Beltrán 2, 46980 Paterna, Spain

[⌈]These authors contributed equaly to this work. *Email: m.vasilopoulou@inn.demokritos.gr, henk.bolink@uv.es, ted.sargent@utoronto.ca

Abstract

Near-infrared light-emitting diodes based on solution-processed semiconductors, such as organics, halide perovskites and colloidal quantum dots, have emerged as a viable technological platform for biomedical applications, night vision, surveillance and optical communications. The recently gained increased understanding of the materials structure-photophysical property relationship has enabled the design of efficient emitters leading to devices with external quantum efficiencies exceeding 20%. Despite significant strides made, challenges remain in achieving high radiance, reducing efficiency roll-off, and extending operating lifetime. This review summarizes recent advances on emissive materials synthetic methods and device key attributes that collectively contribute to improved performance of the fabricated light-emitting devices.

Light-emitting diodes (LEDs) with emission in the near-infrared (NIR) part of the spectrum (700-2500 nm) (termed as NIR-LEDs) support a large variety of applications such as optical diagnosis and biomedical imaging[1], optical communication, remote sensing, security, night vision and data storage[2]. The specific application field determines the spectral range of interest within the NIR (Fig. 1a). With regard to *in vivo* bioimaging, the semi-transparency of biological tissues, oxygenated and deoxygenated blood in specific NIR wavelength regions, also known as biological windows, makes NIR particularly appealing for optical imaging, biomedical sensing and photodynamic therapy. In the field of optical wireless communications, the spectral range is also divided in bands, which correlate with the wavelength regions where optical fibres have small transmission losses[3]. NIR-LEDs are also in demand

for security authentication, optogenetics, life-cycle management of crops, light fidelity and surveillance[4].

Common NIR-LEDs are epitaxial heterostructures of III-V inorganic semiconductors (e.g. GaAs, InGaAs, InGaAlAs)[5-7]. Commercially available products also employ inorganic phosphors, namely compounds doped with transition metals[8], or rare-earth trivalent ions[9]. An external quantum efficiency (EQE) of 72% at 880 nm has been reported for an AlGaAs/GaAs/AlGaAs III-V-LED[6], and 44.5% at 775 nm for LEDs based on $LaMgGa_{11}O_{19}:Cr^{3+}$ phosphors[10]. However, III-V LEDs require post fabrication substrate replacement with high reflective mirror structures to increase their poor power output originating from the refractive index mismatch between those materials (>3.0)[7] and common substrates. Additionally, inorganic phosphors require very high temperature sintering treatment (above 1000 ^{o}C). These processing requirements are an obstacle for low-cost, handheld portable implementations.

Organic (OSCs)[11], metal-halide perovskite (HPs)[12], and colloidal quantum dot (QD)[13] semiconductors, can be processed using low cost and low temperature methods on a wide variety of substrates. For example via solution-based processes such as ink-jet printing, doctor blade and spray coating (Fig. 1b). These qualities make these thin-film LEDs a potentially cost-efficient alternative to their inorganic counterparts and of interest for emerging applications in wearable, implantable and portable electronics. Although there has been progress in different performance metrics such as EQE, challenges remain in reducing the efficiency roll-off, increasing lifetime and to alleviate toxicity issues of some of the emissive materials. In this review, we provide an overview of strategies used to achieve high performance in these thin-film LEDs. The material and device design considerations affecting the peak emission wavelength, efficiency and operational stability are described. We conclude with an outlook on future improvements linked to specific applications.

Toward high-efficiency solution-processed NIR-LEDs

The key performance metrics of a NIR-LED are the EQE, optical output power (P) and radiance (R) (Box 1). The EQE is the product of four parameters namely the probability of electrons and holes recombining (γ), the probability of radiative recombination to occur (r), the photoluminescence quantum yield (PLQY or φ_{PL}) of the emitter and the light outcoupling efficiency (η_{out}) that describes the probability a photon escapes the device in the viewing direction. The parameters r and φ_{PL} are intrinsic properties of the selected emitters, γ also depends on the device configuration and the charge injection interlayers whereas η_{out} depends on the refractive indices of the functional layers and the substrate. To maximize the EQE, it is crucial to simultaneously optimize all four parameters[14-16]. In the following sections, we present the recent progress on the development of narrow bandgap OSC, HP and QD emitters and devices with efficient and stable electroluminescence in the NIR.

Recent progress in NIR organic light-emitting diodes

To maximize organic light-emitting diode (OLED) efficiency, both r and φ_{PL} should approach unity; the latter is defined as the ratio of the radiative (k_r) to total decay rates ($k_r + k_{nr}$). Spin statistics suggest that r is upmost 25% for pure fluorescent emitters and nearly 100% for phosphorescent[17], and thermally activated delayed fluorescent (TADF)[18] ones. Furthermore, *via* triplet-triplet annihilation (TTA), r can reach 25% + 0.5 × 75% = 62.5%[19], under the requirement that the singlet populated states are spin-allowed. Finally, singlet-fission in the presence of a suitable sensitizer can potentially increase r up to 200%[20] (Fig. 2a-c).

To extend the emission of π-conjugated molecules to the NIR, the gap between the highest occupied molecular orbital (HOMO) and lowest unoccupied molecular orbital (LUMO) must be reduced[21]. This can be accomplished by a number of chemical modifications that extend the effective conjugation length

or selectively influence the energy level of the HOMO or the LUMO (Fig. 2d)[22]. The introduction of electron-withdrawing (acceptor) substituents in the aromatic ring can reduce its aromatic character and as a result reduce the electron confinement. Inserting electron-releasing (donor) substituents to a π-conjugated molecule tends to increase the HOMO energy more than that of the LUMO, and as such effectively reducing the gap between them. Another approach relies on the planarization and rigidification of the conjugated system.

However, there is an intrinsic quenching mechanism known as the "energy gap law" according to which, as the energy gap decreases, coupling of the zero-vibration level of the lowest excited state (either singlet, S_1, or triplet, T_1) with the higher vibration levels of the ground state (S_0) promotes non-radiative recombination pathways[23]. The energy gap law induces fundamental constraints on how much the energy gap of OSCs can be effectively decreased, thus limiting the emission of many OSC emitters below 900 nm (Fig. 2e).

Most fluorescent molecules have two electrons in their HOMOs at the ground state, referred to as "a closed shell". Upon excitation, the excited state is either a singlet or triplet. Most organic molecules can only harvest the singlet-excited states radiatively at room temperature, as the transition from a triplet to the ground state is forbidden. This means that these molecules are subjected to r ~25%. As the result, NIR-OLEDs using conventional closed-shell emitters, without assistant's sensitization and in the absence of outcoupling structures or photon recycling, are limited to EQEs of 5%[24,25].

Open-shell radical emitters, have a singly occupied molecular orbital (SOMO) in the ground state, giving an overall spin-1/2 doublet (D_0). If holes and electrons are injected into the HOMO and SOMO, respectively, a fluorescence doublet excited state (D_1) is obtained which gives a spin-allowed emission and r approaches unity (Fig. 2f)[26-28]. One such organic radical, termed as TTM-3NCz, incorporating 3-substituted-9-(naphthalen-2-yl)-9H-carbazole (3NCz) and 3-substituted-9-phenyl-9H-carbazole (3PCz)

added to the tris(2,4,6-trichlorophenyl)methyl (TTM) core, has recently achieved a high φ_{PL} of (85.6 ± 5.4) % when doped in CBP[28]. The fabricated OLEDs emitted at 710 nm with EQEs of 27 and 10% at current densities (J) of $5\text{x}10^{-3}$ and 1 mA cm^{-2}, respectively.

In TADF emitter based LEDs excited long living triplet states can decay *via* the singlet states through reverse intersystem crossing radiatively (Fig. 1a) and as a result, r can approach unity. To enable this process it is essential that the singlet-triplet energy difference (ΔE_{ST}) is small. Generally, ΔE_{ST} is minimized by localizing the HOMO and LUMO orbitals on different fragments of the emitting molecule. This is observed in systems containing spatially separated donor (D) and acceptor (A) heterocycles with twisted linkages. Emission from such molecules occurs from intramolecular charge transfer (CT) states. It is therefore difficult to achieve a low energy gap, small ΔE_{ST} and a large fluorescence rate (k_F) in one molecule[29]. The first successful TADF NIR-OLED employed a phenanthrene-based molecule with a small ΔE_{ST} of 0.13 eV as non-doped emitter; it achieved an EQE of 2.1% at a peak emission of 710 nm[30]. Since then, several studies have also reported NIR electroluminescence (EL) from TADF molecules, albeit with EQE values hardly exceeding 10%[31-34]. These devices were mostly based on multiple donor-acceptor (D_i-A_j) structures. One successful example is an emitter composed of two triphenylamine donor and one acetylacetonate boron difluoride acceptor (inset in Fig. 2g)[32]. This material exhibited a φ_{PL} up to 70% when doped (~6%) in a 4,4′-bis(N-carbazolyl)-1,10-biphenyl (CBP) host (Fig. 2g). The LEDs showed a maximum EQE of 10.0% (at 721 nm) and a high radiance of 3000 W sr^{-1} m^{-2}, albeit at a very high J, of 1000 mA cm^{-2}. Recently, NIR TADF emitters employing simpler D-A structures having strong and planar acceptor units were found to enable *J*-aggregate formation with strong intermolecular CT[35]. Favored by the fast radiative decay rates of the aggregated emitters, the fabricated OLEDs reached an EQE of 14.1% (at 700 nm and J=10^{-2} mA cm^{-2}). Through donor substitution, the intermolecular CT was further strengthened and tuned the OLED

emission at 1010 nm[36]. Similarly, a D-A acenaphthene-based emitter greatly stabilized the intramolecular CT; the fabricated OLEDs displayed a peak EL at 904 nm[37]. Notably, apart from leveraging NIR emission, TADF molecules were recently applied as assistant dopants in hyperfluorescent OLEDs[38,39], demonstrating promising EQEs up to 3.8% (J=5x10^{-2} mA cm^{-2}) with a narrow EL peak (full-width at half-maximum, FWHM, of 40 nm) centered at 840 nm[38].

The most successful examples of NIR OSCs, are organometallic complexes based on third-row transition metal elements, such as platinum (Pt(II)), osmium (Os(II)) and iridium (Ir(III)). In these emitters r = 1 as all the triplet states can decay radiatively at room temperature due to presence of strong spin-orbit coupling enabled by the metal element. So far, Pt(II) phosphors are the most efficient NIR emitters due to the strong metal-metal-to-ligand charge transfer (MMLCT) transition character at the excited state manifolds and the shortest radiative lifetime for phosphorescence[40]. Os(II) phosphors represent the next more efficient class of NIR emitters due to the high metal-to-ligand charge transfer (MLCT) contribution, originating from the lower oxidation potential of the metal d_π orbitals combined with reduced radiative lifetime to sub-microsecond region. In contrast, Ir(III) phosphors present longer radiative lifetime and inferior efficiency compared to Pt(II) and Os(II) ones[41,42]. For example, the state-of-the-art Ir(III)-based NIR-OLEDs have reached a maximum EQE of 9.59% (at 706 nm) by using cyano groups attached in a commercial red emitter **(**Ir(piq)$_2$(acac))[43]. The record performing Os(II)-based NIR-OLEDs employ a series of trans-substituted complexes combining pyrazinyl azolate chelates and dimethyl(phenyl)phosphane ancillaries[44]. They achieved a maximum EQE of 11.5% (at 710 nm), which remained quite high (~8.2%) for a high J=100 mA cm^{-2}. A series of terdentate cyclometallated Pt(II) complexes (PtL^2Cl) of high planarity enabled NIR-OLEDs with a peak excimer emission at ~700 nm and EQE of 14.5%[45].

A breakthrough in NIR-OLEDs was accomplished through the strategic design of a series of 2-pyrazinylpyrazolate Pt(II) fluorinated compounds (1-3) (Fig. 2h); they achieved extraordinary φ_{PL} of 81, 55 and 85% in thin films at peak emission of 740, 703 and 673 nm, respectively (Fig. 2i)[46]. OLEDs based on compound 1 exhibited a remarkable EQE of 24% (at 740 nm) originating from exciton-like emission along the $5d_{z^2}$ direction of edge-on molecular *J*-aggregates. Owing to the short stacking distance in these aggregates, a strong interaction among HOMO and LUMO levels was achieved, which strongly prohibited non-radiative deactivation paths through exciton-optical phonon coupling according to the energy gap law. More recently, the same group demonstrated that delocalized excitonic aggregates can decouple the exciton band from highly vibrational ladders in the ground state, thus further enhancing the φ_{PL} in the NIR region[40,47]. On this basis, they successfully fabricated NIR-OLEDs achieving a high EQE of 2.18% in the NIR region of 890-930 nm[40]; added to the merits, these devices exhibited negligible efficiency roll-off for *J* up to 500 mA cm^{-2}. In a recent work a non-doped EML consisting of only the Pt(II) emitters enabled OLEDs with EQEs > 10 % at 794 nm (J=100 mA cm^{-2})[48], with low efficiency roll-off. Compared with host-guest EML, the complexity is reduced when no host is used, yet the required amount of Pt containing emitters is increased.

Pt-metalloporphyrins also enable NIR electroluminescence with narrow emission spectra. As an example, OLEDs based on Pt(II)–tetraphenyltetrabenzoporphyrin (Pt(tpbp)) presented a NIR emission spectrum centered at 765 nm with a FWHM of ~35 nm and a EQE of 6.3% (J=0.1 mA cm^{-2})[49]. However, porphyrin-based phosphors, typically suffer from efficiency roll-off due to the long-lived triplet exciton resulting in self-quenching. Lanthanide phosphors, such as europium (Er(III)) and niobium (Nd(III)), also exhibit NIR emission bands at the 800-1600 nm spectral region. They originate from efficient energy transfer from the triplet states of the organic ligand to the 4*f* states of the lanthanide core and radiative recombination therefrom. However, the fabricated OLEDs achieved poor

EQEs not exceeding 0.15%[50]. OLEDs based on a rubrene singlet fission sensitizer blended with a phosphorescence emitter (termed as ErQ_3) have also achieved NIR emission centred at 1530 nm[20].

The emergence of NIR perovskite light-emitting diodes

Metal halide perovskites exhibit an AMX_3 chemical structure (Fig. 3a), where A is a monovalent cation (organic, such as methyl ammonium, MA, and formamidinium, FA, or inorganic like cesium, Cs, or their combination), M is a divalent metal such as lead (Pb^{2+}) or tin (Sn^{2+}), and X is a halide (Cl^-, Br^-, I^-). Their advantages for light-emitting applications include facile bandgap tunability through chemical composition, high defect tolerance, symmetric and narrow emission spectra (FWHM<40 nm) and high carrier mobilities[51]; the latter is useful in achieving high brightness at low driving voltages. They can access the 400 to 1100 nm NIR part of the spectrum *via* changes in composition and dimensionality[52-56] (Fig. 3a,b). To optimize the performance of NIR perovskite LEDs (NIR-PeLEDs), it is important to simultaneously maximize the radiative recombination *via* defect passivation while suppressing non-radiative Auger recombination. Three-dimensional (3D) perovskite emitters exhibit fast electron-hole dissociation which decreases the probability of radiative recombination events. Strategies pursuing the confinement of charge carriers *via* dimensionality tailoring, reduction in the grain size and/or film thickness and growth of perovskite nanocrystals (NCs) have been widely explored.

The first successful NIR-PeLED employed a thin (~15 nm) EML of a mixed HP emitter, namely $MAPbI_{3-x}Cl_x$, sandwiched between two charge injection layers[57]. The device achieved an EQE and IQE of 0.76% and 3.4% (at 754 nm), respectively[58]. After this following attempts aimed at increasing the device performance and extending the peak emission wavelength further into the NIR. The most successful approaches include the development of formamidinium-based emitters such as $FAPbI_3$[59-61], Pb-based mixed quasi-two dimensional (2D)/3D perovskites[62,63], mixed Pb-Sn[49] and Pb-free perovskites

with either an organic[50], or inorganic[64], cation at A-site and 2D perovskites[65,66]. Partial or complete replacement of the M-site cation, i.e., Pb^{2+} (ionic radius=1.19 Å), with alternative metals, such as Sn^{2+} and germanium (Ge^{2+}) characterized by smaller ionic radii (1.02 Å and 0.73 Å, respectively), reduced the bandgap and red shifted the emission. For example, systematic replacement of Pb^{2+} with Sn^{2+} in $MAPb_{1-x}Sn_xI_3$ perovskites extended the emission peak from 750 nm (for x=0) to ~950 nm (x=0.8)[50]. The EML, stabilized by incorporating a large cation, e.g., 4-fluorobenzylammonium iodide (FPMAI), exhibited an EQE of 5% (at ~917 nm). A longer NIR emission (at 950 nm) with an EQE of 3.8% was reported for $CsSnI_3$ perovskite[67].

Point defects present in the polycrystalline films, such as A- and X-site vacancies, interstitials and Pb-X anti-sites, act as non-radiative recombination centres and require passivation approaches to suppress electronic trap states and increase φ_{PL} close to unity for efficient NIR-PeLEDs[58-61]. This can be accomplished through the incorporation of passivation agents (PAs) into the precursor solution or *via* post-deposition treatments. Effective passivation materials contain functional groups for coordination to undercoordinated Pb^{2+} or halide ions or ionic bonding to neutralize charged defects[67]. They include Lewis acid and base moieties, alkali metal ions, charged organic components, etc. For example, a breakthrough was achieved by introducing amino-acid additives into the $FAPbI_3$ precursor solutions[58]. These additives passivated surface defects and reduced non-radiative recombination, increasing φ_{PL} to ~70%. Moreover, they led to the spontaneous formation of submicrometre-scale structures (Fig. 3c), which improved the outcoupling efficiency and viewing angle (Fig. 3d). NIR-PeLEDs employing a 3D $FAPbI_3$ perovskite EML achieved an EQE of 20.7% (at 803 nm, J=18 mA cm^{-2})[58]. Notably, these devices showed a high photon flux of 2.33×10^{20} m^{-2} s^{-1} at the peak EQE. Amino-functionalized PAs have also proven effective in suppressing non-radiative recombination in $FAPbI_3$ perovskites[59]. Control over the hydrogen bonding between the functional moieties of the PA and the organic cation of

perovskite led to a record EQE of 21.6% for NIR PeLEDs (at 800 nm, φ_{PL} of 65%, radiance of 308 W sr^{-1} m^{-2}, J = 15.8 mA cm^{-2}).

Improvements in NIR-PeLEDs have also been accomplished using mixed 2D/3D domains that lead to an electron-hole confining cascaded energy landscape (Fig. 3b). Therein, the carrier population is funneled within a few picoseconds to the lowest bandgap domains and remains confined therein such that radiative recombination and EL emission increase[62,63]. The spatial and energy distribution of the different domains within the perovskite films is crucial to maximize a homogeneous energy funnelling to the lowest bandgap light emitting domains. Addition of 1-naphthylmethylamine iodide (NMAI) into a perovskite precursor solution (FAI:PbI_2) resulted in the formation of multiple quantum wells (MQWs) through self-organization[62]. The MQW-based LED exhibited an EQE of 11.7%. This performance originated from highly confined charge carriers within the lower bandgap light-emitting 3D regions by the higher bandgap (2D) regions of the perovskite MQWs. The efficiency of this 2D/3D system was further improved by blending a small fraction of an insulating polymer into the perovskite EML -a technique that has been able to simultaneously reduce non-radiative defects and the refractive index of the perovskite film[63]. The latter also led to an enhanced light outcoupling from PeLEDs. A device using a quasi-2D/3D perovskite ($(NMA)_2(FA)Pb_2I_7$) blended with an insulating polymer (poly(2-hydroxyethyl methacrylate, PHEMA)) showed an EQE of 20.1% (φ_{PL}=96%, EL ~795 nm, J=0.1 mA cm^{-2})[63], representing the best performance 2D/3D HP-based NIR-PeLEDs.

Colloidal HP NCs, pristine[68-70] or metal-doped[71-74], have recently attracted attention due to their advantages of quantum confined emission and low defect density with no shell passivation requirements[68]. NIR-PeLEDs based on $FAPbI_3$ NCs exhibited peak emission at 780 nm with an EQE of 2.3%[69], whereas those using $Cs_xFA_{1-x}Pb(Br_{1-y}I_y)_3$ NCs exhibited a narrow (FWHM ~ 27 nm) NIR emission at 735 nm with an EQE of 5.9%[70]. In another approach, blend EMLs consisted of $FAPbI_3$ NCs

embedded in a molecular matrix that also served as the electron-transporting layer namely 4,4′-diaminodiphenyl sulfone (DDS). In this so-called perovskite-molecule composite (PMC) approach[60], the DDS matrix effectively controlled the nucleation process of the perovskite NCs, leading to the formation of PMC thin films with φ_{PL} approaching 90% (Fig. 3e-g). NIR-PeLEDs with PMC EML achieved an EQE of 17.3% (at 805 nm). Notably, the hybrid perovskite:metal NCs can achieve deeper NIR emission as they rely on energy transfer from the perovskite to the metal and emission therefrom[73]. As an example, ytterbium (Yb^{3+})-doped $CsPbCl_3$ NCs showed NIR emission at 984 nm (EQE of 5.9%)[74].

Progress in NIR QD light-emitting diodes

Colloidal QDs are inorganic semiconductor NCs with emission properties that can be widely tuned through size control due to the quantum confinement effect[75]. They are prepared by wet chemical synthetic procedures that offer precise control over shape and size, which allows them to access the whole NIR spectrum. Their emission tunability can be achieved through increase size and compositional engineering (Fig. 4a)[76]. Lead chalcogenide QDs such as lead sulfide (PbS), selenide (PbSe) and telluride (PbTe), pristine or capped, dominate the NIR applications[77-79]. NIR emission from silicon (Si) QDs has been also observed[80]. The appropriate selection of a wider bandgap inorganic semiconductor shell epitaxially grown around the emissive QD leads to core-shell structures with significantly increased exciton's binding energy[81]. In these structures the electron wavefunction is shifted away from the surface to the QD core reducing non-radiative recombinations. Organic ligands also decorate the core-shell structure (Fig. 4a, inset) to enable solubility in a large variety of non-polar solvents and offer additional surface passivation[82].

In spite of the development of a large variety of NIR emissive QD species, the efficiency of NIR-QDLEDs had been low. This was caused by self-quenching of QDs in the solid state leading to low φ_{PL}

in thin-films combined with moderate carrier mobilities caused by the insulating organic ligands. Auger recombinations are also high in QDs. To mitigate the self-quenching limitation, the first successful NIR-QDLEDs employed EMLs consisted of QDs dispersed into an organic medium or forming a monolayer embedded between two organic interlayers. The operation of these hybrid devices was based on exciton formation in the organic host/surrounding interlayers followed by Förster energy transfer (FRET) to the QDs by means of dipole-dipole interaction. The φ_{PL} of the EML depended critically on this energy transfer step, which should compete against radiative and non-radiative recombination pathways prior to energy transfer. Additionally, the performance of these devices was limited by the low mobility of the organic medium/surrounding interlayers and the lack of materials with suitable energetics to enhance charge injection[83-86]. For example, the first demonstration of a NIR-QDLED was based on core-shell indium arsenide-zinc selenide (InAs-ZnSe) QDs embedded into a poly[2-methoxy-5-(2-ethylhexyloxy)-1,4-phenylenevinylene] (MEH-PPV) matrix[83]. The devices exhibited emission from 1000 to 1300 nm, albeit with low EQE <0.5%.

A breakthrough in NIR-QDLEDs was achieved through the realization of devices using pristine QD-based thick (~40-50 nm) EMLs[87]. Herein, excitons are directly generated on the emissive QDs, thus enhancing the radiative recombination rates. In addition, the charge injection efficiency was separately optimized using appropriate charge-transporting layers. As a result, a device using a neat PbS EML exhibited a maximum EQE of 1.15% (at 1200 nm), representing a significant improvement over previous reports. A further enhancement in NIR-QDLEDs performance was achieved through the precise length control of the organic ligands of PbS QDs[88]. An optimized length of these ligands enabled the simultaneous enhancement in radiative recombinations and carrier mobility in the QD films. Appropriate interlayers injected charges directly to QDs allowing for exciton formation therein and preventing their direct contact with the electrodes, thereby avoiding plasmonic quenching. As a result,

299 an EQE of ~2% (at 1054 nm, J = 1.0 mA cm^{-2}) was obtained. An interlayer engineering approach was
300 also employed in the first reported Si QD NIR-LEDs, which displayed an EQE of 8.6% (at ~850 nm,
301 J=0.01 mA cm^{-2})[89].

302 Some heavy metal-free QDs are considered promising for biological applications. These are either
303 binary, such as silver (Ag) sulfide, selenide and telluride (Ag_2S, Ag_2Se, Ag_2Te), indium phosphide and
304 arsenide (InP, In As), or ternary copper (Cu) or Ag based materials ($CuInSe_2$, $CuInS_2$, $AgInS_2$, $AgInSe_2$)
305 with tunable fluorescent properties and emission maxima up to 1400 nm[90]. However, the reported
306 efficiencies of the fabricated NIR-QDLEDs had been low (<0.5 %[83]). Recently, an efficient heavy
307 metal-free NIR-QDLED was demonstrated using a giant shell In(Zn)As–In(Zn)P–GaP–ZnS QD
308 emitter[91]. Strongly luminescent QDs were prepared through a continuous injection methodology, which
309 enabled a high φ_{PL} of 75% and NIR-LEDs with EQEs of 4.6% (at 857 nm, J = 1.5 mA cm^{-2}). Notably,
310 LEDs with high power and large spectral bandwidth based on InAs/GaAs QDs have also been
311 reported[92]. They achieved strong emission at ~1255 nm, with a maximum output power of 2.6 mW at
312 room temperature.

313 Despite great progress in pristine QD-based NIR-LEDs, optimizing radiative recombination and
314 charge injection/transport simultaneously in these devices is challenging due to their wide bandgap
315 inorganic shells and long-chain organic ligands, which impede carrier transport in the neat QD film [93-98].
316 Recently, this issue was successfully addressed by following a QD-in-perovskite approach using hybrid
317 EMLs consisting of QD emitters evenly distributed in a perovskite transport medium[99,100]. Unlike prior
318 approaches, where QDs were either enclosed in a protective shell and/or insulating ligand or dispersed in
319 a low mobility organic medium, here, PbS QDs were embedded in a high mobility $MAPbI_xBr_{3-x}$
320 perovskite matrix, which epitaxially grew around the QD surface also acting as an efficient surface
321 passivation agent. This hybrid system benefitted from the high φ_{PL} of QDs and the superior carrier

mobility of the perovskite medium. The halide ratio in the perovskite was finely tuned in order to avoid lattice mismatch leading to defect sites that would act as traps for non-radiative recombination (Fig. 4b,c)[99]. QD-in-perovskite LEDs achieved 150×higher EQE (5.2%, emission peak at 1391 nm) and 15×higher brightness (2.6 W sr^{-1} m^{-2} at 3.5 V) than a control QD-only LED.

This approach was further optimized through the incorporation of PbS QDs in a low-dimensional layered perovskite[101]. The number of perovskite repeated units <*n*> confined between bulk organic cations determined the bandgap and exciton binding energy of the resultant QW. This allowed transitioning from a fully excitonic character (*n* = 1, 2) to a mixed scenario where free charges and excitons coexist (n > 2). This was leveraged to manipulate energy transfer into the QDs achieving balanced charge transport into the QD emitters and hence minimizing Auger recombination. The devices achieved tunable emission in the 980-1600 nm spectral region with a maximum EQE of 8.1% (at 980 nm, J = 1.65 mA cm^{-2}, radiance of 7.4 W sr^{-1} m^{-2}). In another case, non-toxic silicon dioxide (SiO_2)-encapsulated Ag_2S QDs were epitaxially dispersed in a caesium-containing triple cation perovskite matrix[102]. The optimized NIR-LEDs demonstrated an EQE of 17.0% (at 1397 nm, J = 11.28 mA cm^{-2}), originating from charge balance close to unity enabled by a thin porphyrin hole-transporting interlayer that also protected the perovskite matrix from metal oxide (i.e., molybdenum oxide)-induced degradation.

A different approach employed an EML that comprised of a ternary blend including a binary host matrix and the QD emitters. This matrix consisted of small size, wide bandgap PbS QDs that electronically passivated the larger size, low bandgap PbS QD emitters blended with zinc oxide (ZnO) NCs to balance carrier supply[103]. The larger size emitters exhibited reduced non-radiative recombination rates and balanced charge injection (Fig. 4d-f). The fabricated QDLEDs showed a peak emission at 1400 nm with an EQE of ~7.9%, which is the highest reported value for any NIR-QDLED based on a

neat QD EMLs. The same authors have recently achieved a higher EQE of 8.0% through further engineering at the supra-nanocrystalline level and optimization of charge carrier balance within the device[104].

Comparison between different solution-processed NIR LEDs

OLEDs and PeLEDs have already achieved high EQEs over 20% at wavelengths <1000 nm whereas QDLEDs can span a larger part of the NIR spectrum with emission up to 1500 nm, albeit with lower efficiencies (Fig. 5a, Supplementary Table 1). Metal halide perovskites and QDs generally enable response speeds of ~100 ns[105,106], whereas OSCs based on CT states have reached response times of 14.7 ns[107]. However, hybrid perovskite-polymer materials have reached high speeds of 5 ns[108], whereas QDs recently attained an ultra-fast response of 74 ps (FWHM)[109], by allowing carriers to be swept to the electrodes before they fall into the band tail states; these values indicate that these solution-based semiconductors will be soon appropriate for NIR-applications with high speed requirements. Device engineering and the design and development of novel emitters have played a crucial role to reach such performance.

Interface engineering and light outcoupling approaches

The aforementioned classes of NIR-LEDs require similar architectural design considerations that mainly target the reduction of charge-injection barriers, blocking of carrier leakage, and exciton confinement within the EML. They have all benefitted from a rich knowledge gathered through progress in visible OLEDs from which they have borrowed charge-transporting interlayers, such as organic small molecules, polymers and metal oxides with appropriate energy landscapes. Extra caution, however, should be paid as physicochemical interactions between these materials and novel emitters, for example,

368 perovskite ones, may negatively impact on the device performance and reliability[110]. Besides high
369 efficiency, other device performance metrics such as EQE-roll-off and operational lifetime are improved
370 through interface engineering as explained in the next sections.

371 Light trapping is a critical factor that restricts the thin-film LEDs efficiency. For example, the
372 high EQE of GaAs NIR-LEDs (~72%[6]) would be <5% without the application of complex mirror
373 structures to extract light in the viewing angle. The low outcoupling efficiency of thin-film LEDs is due
374 to the waveguide modes in the multilayered sandwich structures and plasmonic quenching at the
375 metallic electrode. In addition, the photon reabsorption by the EML and the low transmittance of
376 indium-tin-oxide (ITO) transparent electrode also contribute to efficiency losses. The waveguide modes
377 have the major contribution in light propagation losses; they divide into the glass total internal reflection
378 and the ITO/functional layers guided mode. They are regulated by Snell's law according to the refractive
379 indices of the EML (i.e., 1.7-2.0 for OSCs[111], and >2.0 for perovskites and QDs[111,112]), ITO (~2.0), glass
380 substrate (1.5) and ambient air (1.0), with the η_{out} of these devices to be limited at 20-25%. Due to the
381 high refractive indices of perovskites and QDs compared with those of the substrate and the commonly
382 used charge-transporting interlayers, a large portion of the generated light is confined in the EML and
383 propagates in the lateral direction, which further compromises η_{out}.

384 To enhance light-outcoupling, numerous low-cost methods have been advanced, including patterned
385 or roughened substrates using wet-etching methods or insertion of low-index materials on the
386 substrate/air interface to extract substrate modes, low-index grids and index-matched functional layers
387 for extracting waveguide modes and corrugated metal electrodes for plasmonic modes[111]. However,
388 adopting simpler methods such as manipulating the emitter's morphology[113], inducing spontaneous
389 formation of submicrometre-scale structures[58], enhancing horizontal orientation of emissive dipoles[46],
390 applying cavity engineering and top emitting devices[114,115], using small-thickness emissive layers[116],

391 tuning the width in MQW structures[111,114] or enhance photon-recycling[117], can beneficially influence
392 light extraction without increasing device fabrication cost and complexity.
393
394 **Low power output, EQE roll-off and lifetime in solution-processed NIR LEDs**
395 To meet the technical specifications of III-V LEDs for commercial applications, these solution-
396 processed NIR-LEDs need a stable power output of ~10-100 mW for λ<1000 nm and up to several mW
397 for λ>1200 nm (at a J of 1000-2000 mA cm^{-2}). For example, for surveillance or night vision applications
398 (850-900 nm) the requirements are for a power output of 10-100 mW, which is equivalent to an
399 irradiance of 10^3-10^4 mW cm^{-2}. For bio-imaging in the first and second biological windows (Fig. 1a), the
400 requirements are for 10-100 mW cm^{-2} dependent on the wavelength of interest. The recent developments
401 in all three classes of the solution-processed NIR-LEDs indicate that these devices will soon have the
402 potential for applications with lower power output demands such as bioimaging.
403 Another major issue in all LED technologies is the drop of EQE at high J, the so-called EQE roll-off,
404 which has been generally attributed to charge imbalance, field-induced quenching of luminescence,
405 Auger recombination and Joule heating[118]. The significant EQE-roll-off also indicates that these devices
406 are subjected to increased electrical stress to achieve a given radiance, which in-turn reduces the useful
407 lifetime; that is the time after which the radiance (or EQE) drops below a predefined level. In OLEDs, in
408 particular, as the carrier concentration increases, the bound electron-hole pairs or excitons get
409 annihilated[119] and EQE typically drops at J>100 mA cm^{-2}. Apart from these reasons, notable underlying
410 processes for such efficiency loss are singlet-triplet and triplet-triplet annihilation, as well as host-
411 induced quenching (in doped OLEDs)[120]. Through careful design of novel emitters, judicious
412 engineering of the host-guest system and adoption of non-doped EMLs based on J-aggregated emitters,
413 suppression of various inherent loss processes has been achieved. We note, the exceptional examples of

NIR-OLEDs based on the boron difluoride curcuminoid TADF emitter[32], or on Pt(II) complexes forming *J*-aggregates[40], which showed negligible EQE roll-off for *J* values up to 700 and 500 mA cm^{-2}, respectively (Fig. 5b). Moreover, OLEDs have demonstrated moderate lifetime of ×100-1000 h, however, at *J*<50 mA cm^{-2} (Figure 5c,d, Supplementary Table 2). Notorious reasons for low lifetime are exciton quenching mechanisms explained above, presence of impurities in the EML, appearance of dark spots, oxidation, corrosion, and electrochemical degradation all caused by the attack of moisture[121]. Besides successful encapsulation, device engineering targeting to alleviate exciton quenching and broaden the emission zone significantly boosts operational stability[24]. For example, incorporation of diketopyrrolopyrrole emitters in a polymer medium demonstrated OLEDs with improved durability[119]. Nevertheless, the device stability will need to be improved to enable practical applications (> 10000 h depending on the type of application). Encouraging in these regards are the OLEDs using wide bandgap perovskite charge-injection interlayers[122].

QDLEDs suffer from severe EQE roll-off [103] (Fig. 5b), which originates, apart from charge injection imbalance and Auger recombination rates, by the formation of electric-fields inside the QDs known as quantum-confined stark effect (QCSE)[123]. This causes a red shift of the exciton emission energy accompanied with a strong separation of electron-hole wavefunctions that dramatically decreases luminescence efficiency. When QDs are dispersed in a high mobility perovskite matrix this phenomenon is suppressed due to increase in the carrier density that screens the QD field. Reduced Auger recombination is also expected in the QD-in-perovskite architecture due to the epitaxial passivation provided by the perovskite matrix and reduced energetic disorder, ultimately promoting radiative decay pathways[124]. For example, the incorporation of PbS QDs in a quasi-2D perovskite EM[101] has been reported to result in balanced charge injection up to high currents nearing *J* = 170 mA cm^{-2}. The devices showed a maximum EQE of ~8% and threshold current density (J_0, corresponding to 50% EQE drop)

approaching 400 mA cm^{-2}. This approach has also led to improved operational stability as the main device degradation mechanisms have been alleviated (Fig. 5c,d). QDLEDs using a binary blend of small and large-size PbS QDs exhibited an estimated T_{50} of more than 26000 h (at initial radiance of 1 W sr^{-1} m^{-2})[104], paving the way for durable QDLEDs operating at low brightness.

Perovskites possess high carrier mobilities compared to OSCs and QDs which implies that charges are spread uniformly in the EML even at higher *J*, mitigating Auger recombination[125]. Therefore, NIR-PeLEDs show a lower EQE roll-off and a J_0 between 300-1500 mA cm^{-2}. For example, PeLEDs employing a 3D perovskite $Cs_{0.17}FA_{0.83}PbI_{2.5}Br_{0.5}$ with an excess of FAI as the EML showed an EQE of 17.4% with a negligible roll-off up to J=600 mA cm^{-2} (Fig. 5b)[61]. Similarly, PeLEDs based on 2D perovskites retained a nearly stable EQE for J=1500 mA cm^{-2} (Fig. 5b)[65]. The observed EQE roll-off in these devices is due to Joule heating, a mechanism that is more critical for PeLEDs than for other types of LEDs. In fact, even small temperature changes significantly affect the device efficiency and induce severe EQE roll-off[116]. Joule heating originates from inefficient charge injection into the EML, conductivity mismatch between the perovskite and charge-transporting interlayers and poor perovskite film morphology that can increase series resistance. Selecting suitable interlayers pristine or doped[126,127], optimizing the device geometry, using sapphire substrates to better dissipate heat or attaching heat spreaders and sinks, downscaling the device active area or driving these LEDs with current pulses are few of the adopted thermal management strategies[128,129]. For example, through employing a polymer hole-transporting layer with high ionization energy, large-area (900 mm^2) NIR PeLEDs emitting at 799 nm with a high EQE of 12.1% (EQE of small area devices 20.2%), were successfully demonstrated[127]. Higher lifetime is generally accomplished in pure-phase 2D, mixed phased 2D/3D and passivated 3D PeLEDs where mobile ions and defects are significantly suppressed[130-133]. Alleviating Joule heating and interface degradation[132,134] has prolonged PeLEDs lifetime considerably.

Issues with some of the emitters

The presence of toxic elements, such as Pb in HPs and Cd in QDs[135], and high costs of noble metals in phosphorescent complexes, raises concerns about the suitability of such materials for consumer electronics. The European Restriction of Hazardous Substances Directive (RoHS) has set strict rules about the use of toxic elements in electronic equipment. The current limit is 1000 ppm for Pb and 100 ppm for Cd by weight of solid device components. Commercially available QD TV displays use QD quantities within the RoHS limits (a 55-inch display requires about 1.5 mg of Cd). This will also stand for perovskites which possess identical extinction coefficient (of the order of 10^5 cm^{-1} M^{-1}) with QDs and similar φ_{PL} at the same emission wavelengths (530 and 630 nm). Although efforts to find environmentally benign alternatives are also underway, up to now OLEDs based on fluorescent and TADF emitters are the elective choice for *in vivo* biomedical applications, where the material's low toxicity is an advantage.

Outlook and future directions

The inherent suitability of solution-processed semiconductors for large area applications allows unparalleled design freedom in developing novel concepts in illumination systems. As highlighted in this review, large progress in the development of narrow bandgap emissive materials and device engineering has already been accomplished in recent years leading to high-performance solution-processed NIR-LEDs. Primary challenges still remain in terms of high radiance, especially in the longer wavelength range, and long operation stability.

Challenges associated with pristine emitters-Towards hybrid materials?

From a material engineering point of view, synthetic approaches have recently contributed towards the improved device performance as they led to emitters with radiative efficiency approaching unity. However, intrinsic material limitations pose restrictions on how much the bandgap of OSCs and HPs can be effectively decreased constituting their emission efficient for wavelengths up to 1000 nm for the former and below 900 nm for the latter class. QDs can efficiently span most of the NIR spectrum through the size confinement effect; albeit with lower efficiencies.

Appropriate manipulation in the chemical design of OSCs and chromophores has led to some notable performance levels in OLEDs in the 700-1000 nm wavelength region. Extending their luminescence into the IR can be pursued by the design of molecules possessing a shallow potential energy surface (PES) in their ground state, so that non-radiative recombinations originating from high-frequency vibrational quenching would be significantly suppressed. Alternatively, *J*-aggregated emitters allowing long wavelength emission from CT states also offer a viable path to significantly red shift the emission wavelengths without compromising the device efficient and stable operation.

Perovskites show high performance levels with narrow emission spectra, albeit at shorter wavelengths in the NIR region. Control over their composition/dimensionality raises the prospect of further expanding their luminescence efficiency. Moreover, most of the passivation methods applied to tackle the high defect density issue were borrowed from the solar cell research community using trial-and-error approaches. With the increased demand for extended stability, these approaches are now starting to reach their limits such that future major advances will require new methodologies that can analyse the material and device characteristics and establish useful guidelines for rational device optimization.

The unique optical properties of colloidal QDs have motivated an early surge of interest for their application in NIR-LEDs. However, the low carrier mobility of thin-film QDs has precluded the

achievement of high-performance. The recently proposed ternary QD and QD-in-perovskite hybrid solutions offer a promising path to overcome this limitation, enabling QDLEDs with performance metrics similar to those of OLEDs and PeLEDs at much longer wavelengths. These hybrid approaches are characterized by the simultaneous achievement of high mobility and enhanced non-radiative recombination rates not observed in independent QD emitters. Therefore, the hybrid systems offer all the advantages of individual counterparts, including the long wavelength emission, and are likely to play a central role in the next generation of NIR-LEDs.

The hybrid materials can indeed create functionalities that couldn't have been possible otherwise. Apart from the QD-in-perovskite approach, the perovskite-organic molecule composite represents a nice example of how to overcome the weaknesses and strengthen the advantages of individual components to some extent. In the same direction, could be the implementation of high mobility ambipolar perovskite host matrices combined with *J*-aggregated or open-shell OSCs to alleviate constraints relative to poor charge mobility of the latter. Inclusion of perovskite single crystals into conjugated polymer matrices to form EMLs with a continuous transport phase or substitution of insulating ligands of QDs with high mobility OSCs directly anchored onto the QD surface are some examples that might offer viable future solutions. An added advantage to these hybrid materials is offered from the inherent solution-processability of the individual components that facilitates their easy integration into devices and systems to eventually transform present materials and prototypes into a promising technology.

Limitations associated with the device design and operation

From the device engineering point of view, significant progress has already been made based on advances in charge-transporting interlayers developed for the more mature visible emitting OLED and QDLED technologies. However, extra caution is needed prior to the application of conventional and

novel interfacial materials in devices embedding HPs due to the suspected physicochemical interaction at the heterointerfaces. Moreover, since the commonly used ITO transparent electrode presents high absorption in the NIR, considering its replacement with alternative electrodes, such as silver nanowires[136], will offer advantages with respect to high efficiency and cost-effectiveness.

Challenges remain when targeting high and stable power output. Significant efficiency roll-off at elevated *J* and moderate lifetimes below the 10000 h target remain key obstacles prior to the commercialization of these devices. Besides the design of novel emitters, ingenious device engineering, suitable encapsulation, successful management of thermal and electrical stress will prolong the device lifespan considerably as they successfully counter the intrinsic and extrinsic degradation mechanisms. To conclude, LEDs based on OSCs, HPs and QDs pristine and hybridized are suitable for many established and emerging NIR lighting applications. There are of course important challenges ahead. As research continues to progress both in the development of novel emitters and devices, we can expect even more advanced performances through deepen physical understanding and optimization of each technology combined with fruitful interactions and increased influence between them.

REFERENCES

1. Gu, Y. Y. et al. High-sensitivity imaging of time-domain near-infrared light transducer. *Nat. Photonics* **13**, 525–531 (2019).

2. Smith, A. M., Mancini, M. C. & Nie, S. Second window for in vivo imaging. *Nat. Nanotechnol.* **4**, 710–711 (2009).

3. Ramaswami, R. Optical fiber communication: from transmission to networking. *IEEE Commun. Mag.* **40**, 138–147 (2002).

4. Wu, X. et al. Dye-sensitized core/active shell upconversion nanoparticles for optogenetics and bioimaging applications. *ACS Nano* **10**, 1060–1066 (2016).

5. Mokkapati, S. & Jagadish, C. III-V compound SC for optoelectronic devices. *Mater. Today* **12**, 22–32 (2009).

6. Schnitzer, I., Yablonovitch, E., Caneau, *C. &* Gmitter. T. J. Ultrahigh spontaneous emission quantum efficiency, 99.7% internally and 72% externally, from AlGaAs/GaAs/AlGaAs double heterostructures. *Appl. Phys. Lett*. **62**, 131 (1993).

7. Broell, M., Sundgren , P., Rudolph , A., Schmid, W., Vogl, A. & Behringer, M. New developments on high efficiency infrared and InGaAlP light emitting diodes at OSRAM opto-semiconductors. *Proc. of SPIE* **9003**, 90030L (2014).

8. Mao, M. et al. Broadband near-infrared (NIR) emission realized by the crystal-field engineering of $Y_{3-x}Ca_xAl_{5-x}S_{ix}O_{12}:Cr^{3+}$ (x = 0–2.0) garnet phosphors. *J. Mater. Chem. C* **8**, 1981–1988 (2020).

9. Zhong, Y. & Dai, H., A mini-review on rare-earth down-conversion nanoparticles for NIR-II imaging of biological systems. *Nano Res.* **13***,* 1281–1294 (2020).

10. Liu, S., Wang, Z., Cai, H., Song, Z. & Liu, Q. Highly efficient near-infrared phosphor $LaMgGa_{11}O_{19}:Cr^{3+}$. *Inorg. Chem. Front.* **7**, 1467–1473 (2020).

11. Zampetti, A.; Minotto, A. & Cacialli, F. Near-infrared (NIR) organic light-emitting diodes (OLEDs): Challenges and opportunities. *Adv. Funct. Mater.* **29**, 1807623 (2019).

12. Kumawat, N. K., Dey, A., Narasimhan, K. L. & Kabra, D., Near infrared to visible electroluminescent diodes based on organometallic halide perovskites: structural and optical investigation. *ACS Photonics* **2**, 349–354 (2015).

13. Sargent, E. H., Infrared quantum dots. *Adv. Mater.* **17**, 515–522 (2005).

14. Mikhnenko, O. V., Blom, P. W. M. & Nguyen, T.-Q. Exciton diffusion in organic semiconductors. *Energy Environ. Sci.* **8**, 1867–1888 (2015).

15. Voznyy, O., Sutherland, B. R., Ip, A. H., Zhitomirsky, D. & Sargent, E. H. Engineering charge transport by heterostructuring solution-processed semiconductors. *Nat. Rev. Mater.* **2**, 17026 (2017).

16. Liu, X.-K., Xu, W., Bai, S., Jin, Y., Wnag, J., Friend, R. H. & Gao, F. Metal halide perovskites for light-emitting diodes. *Nat. Mater.* **20**, 10–21 (2021).

17. Zhang, Y. et al. Near-infrared emitting materials *via* harvesting triplet excitons: Molecular design, properties, and application in organic light emitting diodes. *Adv. Opt. Mater.* **6**, 1800466 (2018).

18. Uoyama, H., Goushi, K., Shizu, K., Nomura, H. & Adachi, C. Highly efficient organic light-emitting diodes from delayed fluorescence. *Nature* **492**, 234–238 (2012).

19. Adachi, C. Third-generation organic electroluminescence materials. *Jpn. J. Appl. Phys.* **53**, 060101 (2014).

20. Nagata, R., Nakanotani, H., Potscavage Jr., W. J. & Adachi, C. Exploiting singlet fission in organic light-emitting diodes. *Adv. Mater.* **30**, 1801484 (2018).

21. Narsaria, A. K., Poater, J., Guerra, C. F., Ehlers, A. W., Lammertsma, F. M., Rational design of near□infrared absorbing organic dyes: Controlling the HOMO–LUMO gap using quantitative molecular orbital theory. *J. Comput. Chem.* **39**, 2690–2696 (2018).

22. Roncali, J. Molecular engineering of the band gap of π□conjugated systems: facing technological applications. *Macromol. Rapid Commun.* **28**, 1761–1775 (2007).

23. Englman, R. & Jortner, J. The energy gap law for radiationless transitions in large molecules. *Mol. Phys.* **18**, 145–164 (1970).

24. Minotto, A. et al. Efficient near-infrared electroluminescence at 840 nm with "metal-free" small-molecule:polymer blends. *Adv. Mater.* **30**, 1706584 (2018).

25. Minotto, A. et al. Towards efficient near-infrared fluorescent organic light-emitting diodes. *Light Sci. Appl.* **10,** 18 (2021).

26. Peng, Q., Obolda, A., Zhang, M. & Li, F. Organic light-emitting diodes using a neutral π radical as emitter: The emission from a doublet. *Angew. Chem. Int. Ed.* **54**, 7091–7095 (2015).

27. Guo, H. et al. High stability and luminescence efficiency in donor–acceptor neutral radicals not following the Aufbau principle. *Nature Mater.* **18**, 977–984 (2019).

28. Ai, X. et al. Efficient radical-based light-emitting diodes with doublet emission. *Nature* **563**, 536–540 (2018).

29. Yamanaka, T., Nakanotani, H., Hara, S., Hirohata, T. & Adachi, C. Near-infrared organic light-emitting diodes for biosensing with high operating stability. *Appl. Phys. Express* **10**, 074101 (2017).

30. Wang, S. et al. Highly efficient near-infrared delayed fluorescence organic light emitting diodes using a phenanthrene-based charge-transfer compound. *Angew. Chem. Int. Ed.* **54**, 13068–13072 (2015).

31. Yuan, Y. et al. Over 10% EQE near-infrared electroluminescence based on a thermally activated delayed fluorescence emitter. *Adv. Funct. Mater.* **27**, 1700986 (2017).

32. Kim, D. H. et al. High-efficiency electroluminescence and amplified spontaneous emission from a thermally activated delayed fluorescent near-infrared emitter. *Nat. Photonics* **12**, 98–104 (2018).

33. Ye, H. et al. Near-infrared electroluminescence and low threshold amplified spontaneous emission above 800 nm from a thermally activated delayed fluorescent emitter. *Chem. Mater.* **30**, 6702-6710 (2018).

34. Hu, Y. Yuan, Y., Shi, Y.-L., Li, D., Jiang, Z.-Q. & Liao, L.-S. Efficient near□infrared emission by adjusting the guest–host interactions in thermally activated delayed fluorescence organic light□emitting diodes. *Adv. Funct. Mater.* **28**, 1802597 (2018).

618 35. Xue, J. et al. Highly efficient thermally activated delayed fluorescence via *J*-aggregates with
619 strong intermolecular charge transfer. *Adv. Mater*. **31**, 1808242 (2019).
620 36. Liang, Q., Xu, J., Xue, J. & Qiao, J. Near-infrared-II thermally activated delayed fluorescence
621 organic light-emitting diodes. *Chem. Commun.* **56**, 8988–8991 (2020).
622 37. Congrave, D. G. et al. A simple molecular design strategy for delayed fluorescence toward 1,000
623 nm. *J. Am. Chem. Soc.* **141**, 46, 18390–18394 (2019).
624 38. Shahalizad, A. et al. Efficient solution-processed hyperfluorescent OLEDs with spectrally narrow
625 emission at 840 nm. *Adv. Funct. Mater*. **31**, 2007119 (2021).
626 39. Brodeur, J., Hu, L., Malinge, A., Elad Eizner, E., Skene, W. G. & Kéna-Cohen. S. Highly efficient
627 and spectrally narrow near-infrared fluorescent OLEDs using a TADF-sensitized cyanine dye. *Adv.*
628 *Optical Mater*. **7**, 1901144 (2019).
629 40. Wei, Y. C. *et al.* Overcoming the energy gap law in near-infrared OLEDs by exciton–vibration
630 decoupling. *Nat. Photonics* **14,** 570–577 (2020).
631 41. Xue J. et al. Homoleptic facial Ir(III) complexes *via* facile synthesis for high-efficiency and low-
632 roll-off near-infrared organic light-emitting diodes over 750 nm. *Chem. Mater.* 29, 4775−4782 (2017).
633 42. Lee, T.-C. et al. rational design of charge□neutral, near□infrared□emitting osmium(II) complexes
634 and OLED fabrication. *Adv. Funct. Mater.* 19, 2639-2647 (2009).
635 43. Chen, Z. et al. A simple and efficient approach toward deep-red to near-infrared-emitting iridium(III)
636 complexes for organic light-emitting diodes with external quantum efficiencies of over 10%. *Chem. Sci.* **11**,
637 2342-2349 (2020).
638 44. Yuan, Y., Liao, J.-L., Ni, S.-F., Je, A. K.-Y., Lee, C.-S. & Chi, Y. Boosting efficiency of near□
639 infrared organic light□emitting diodes with Os(II)□based pyrazinyl azolate emitters. *Adv. Funct. Mater.*
640 30, 1906738 (2020).

641 45. Cocchi, M., Kalinowski, J., Virgili, D. & Williams, J. A. G. Excimer-based red/near-infrared
642 organic light-emitting diodes with very high quantum efficiency. *Appl. Phys. Lett.* **92**, 113302 (2008).
643 46. Tuong Ly, K. et al. Near-infrared organic light-emitting diodes with very high external quantum
644 efficiency and radiance. *Nat. Photonics* **11**, 63–68 (2017).
645 47. Chen, W.-C. et al. Modulation of solid□state aggregation of square□planar Pt(II) based emitters:
646 enabling highly efficient deep□red/near infrared electroluminescence. *Adv. Funct. Mater.* **30**, 2002494
647 (2020).
648 48. Wang, S. F. et al. Highly efficient near-infrared electroluminescence up to 800 nm using
649 Platinum(II) phosphors. *Adv. Funct. Mater*. **30**, 2002173 (2020).
650 49. Borek, C. et al. Highly efficient, near-infrared electrophosphorescence from a Pt–metalloporphyrin
651 complex. *Angew. Chem. Int. Ed.* **46**, 1109–1112 (2007).
652 50. Jinnai, K., Kabe, R. & Adachi, C. A near-infrared organic light-emitting diode based on an Yb(III)
653 complex synthesized by vacuum co-deposition. *Chem. Commun.* 53, 5457–5460 (2017).
654 51. Sutherland, B. R. & Sargent, E. H. Perovskite photonic sources. *Nat. Photonics* **10**, 295–302
655 (2016).
656 52. Qiu, W. *et al.* Mixed lead–tin halide perovskites for efficient and wavelength-tunable near-infrared
657 light-emitting diodes. *Adv. Mater.* **31**, 1806105 (2019).
658 53. Lai, M. L. *et al.* Tunable near-infrared luminescence in tin halide perovskite devices. *J. Phys.*
659 *Chem. Lett.* **7**, 2653–2658 (2016).
660 54. Smith, M. D., Connor, B. A. & Karunadasa, H. I. Tuning the luminescence of layered halide
661 perovskites. *Chem. Rev.* **119**, 3104–3139 (2019).
662 55. Akkerman, Q. A., Rainò, G., Kovalenko, M. V. & Manna, L. Genesis, challenges and
663 opportunities for colloidal lead halide perovskite nanocrystals. *Nat. Mater.* **17**, 394–405 (2018).

56. G. Xing, *et al.* Low-temperature solution-processed wavelength-tunable perovskites for lasing. *Nat. Mater.*, **13** 476–480 (2014).

57. Z.-K. Tan, *et al.* Bright light-emitting diodes based on organometal halide perovskite. *Nat. Nanotechnol.*, 9, 687–692 (2014).

58. Cao, Y. *et al.* Perovskite light-emitting diodes based on spontaneously formed submicrometre-scale structures. *Nature* **562**, 249–253 (2018).

59. Xu, W. *et al.* Rational molecular passivation for high-performance perovskite light-emitting diodes. *Nat. Photon.* **13**, 418–424 (2019).

60. Wang, H. *et al.* Perovskite-molecule composite thin films for efficient and stable light-emitting diodes. *Nat. Commun.* **11**, 891 (2020).

61. Jia, Y.-H. *et al.* Role of excess FAI in formation of high-efficiency $FAPbI_3$-based light-emitting diodes. *Adv. Funct. Mater.* **30**, 1906875 (2020).

62. Wang, N. *et al.* Perovskite light-emitting diodes based on solution-processed self-organized multiple quantum wells. *Nat. Photonics* **10**, 699–704 (2016).

63. Zhao, B. *et al.* High-efficiency perovskite-polymer bulk heterostructure light-emitting. *Nat. Photonics* **12**, 783–789 (2018).

64. Hong, W.-L. *et al.* Efficient low-temperature solution-processed lead-free perovskite infrared light-emitting diodes. *Adv. Mater.* **28**, 8029–8036 (2016).

65. Yang, R. *et al.* Oriented quasi-2D perovskites for high performance optoelectronic devices. *Adv. Mater.* **30**, 1804771 (2018).

66. Tsai, H. *et al.* Stable light-emitting diodes using phase-pure Ruddlesden–Popper layered perovskites. *Adv. Mater.* **30**, 1704217 (2018).

686 67. Giuri, A. *et al.* Ultra-Bright Near-infrared perovskite light-emitting diodes with reduced efficiency
687 roll-off. *Sci. Rep.* **8**, 15496 (2018).
688 68. Kovalenko, M. V., Protesescu, L. & Bodnarchuk, M. I. Properties and potential optoelectronic
689 applications of lead halide perovskite nanocrystals. *Science* **358**, 6364, 745–750 (2017).
690 69. Protesescu, L. et al. Dismantling the "red wall" of colloidal perovskites: highly luminescent
691 formamidinium and formamidinium–cesium lead iodide nanocrystals. *ACS Nano* **11**, 3, 3119–3134
692 (2017).
693 70. Lignos, I. et al. Exploration of near-infrared-emissive colloidal multinary lead halide perovskite
694 nanocrystals using an automated microfluidic platform. *ACS Nano* **12**, 6, 5504–5517 (2018).
695 71. Pan, G. *et al.* Doping lanthanide into perovskite nanocrystals: Highly improved and expanded
696 optical properties. *Nano Lett.* **17**, 8005–8011 (2017).
697 72. Shen, X. *et al.* Zn-alloyed $CsPbI_3$ nanocrystals for highly efficient perovskite light-emitting
698 devices. *Nano Lett.* **19**, 1552–1559 (2019).
699 73. Milstein, T. J., Kroupa, D. M. & Gamelin, D. R. Picosecond quantum cutting generates
700 photoluminescence quantum yields over 100% in ytterbium-doped $CsPbCl_3$ nanocrystals. *Nano Lett.* **18**,
701 3792–3799 (2018).
702 74. Ishii, A. & Miyasaka, T. Sensitized Yb^{3+} luminescence in $CsPbCl_3$ film for highly efficient near-
703 infrared light-emitting diodes. *Adv. Sci.* **7**, 1903142 (2020).
704 75. Shirasaki, Y., Supran, G. J., Bawendi, M. G. & Bulovic, V. Emergence of colloidal quantum-dot
705 light-emitting technologies. *Nat. Photonics* **7**, 13–23 (2013).
706 76. Ma, Y., Zhang, Y. & Yu, W. W. Near infrared emitting quantum dots: synthesis, luminescence
707 properties and applications. *J. Mater. Chem. C* **7**, 13662–13679 (2019).

77. Rogach, A. L. et al. Colloidally prepared HgTe nanocrystals with strong room□temperature infrared luminescence. *Adv. Mater.* **11**, 552–555 (1999).

78. Harrison, M. T. et al. Wet chemical synthesis of highly luminescent HgTe/CdS core/shell nanocrystals. *Adv. Mater.* **12**, 123–125 (2000).

79. Harris, D. K. et al. Synthesis of cadmium arsenide quantum dots luminescent in the infrared. *J. Am. Chem. Soc.* **133**, 4676–4679 (2011).

80. Cheng, K.-Y., Anthony, R., Kortshagen, U. R. & Holmes, R. J. Hybrid silicon nanocrystal-organic light-emitting devices for infrared electroluminescence. *Nano Lett.* **10**, 1154–1157 (2010).

81. Tang, R. et al. Tunable ultrasmall visible-to-extended near-infrared emitting silver sulfide quantum dots for integrin-targeted cancer imaging. *ACS Nano* **9**, 220–230 (2015).

82. Hinds, S. et al. NIR-emitting colloidal quantum dots having 26% luminescence quantum yield in buffer solution. *J. Am. Chem. Soc.* **129**, 7218–7219 (2007).

83. Tessler, N., Medvedev, V., Kazes, M., Kan, S. & Banin, U. Efficient near-infrared polymer nanocrystal light-emitting diodes. *Science* **295**, 1506–1508 (2002).

84. Steckel, J. S., Coe-Sullivan, S., Bulovic, V. & Bawendi, M. G. 1.3 μm to 1.55 μm Tunable electroluminescence from PbSe quantum dots embedded within an organic device. *Adv. Mater.* **15**, 1862–1866 (2003).

85. Konstantatos, G., Huang, C. J., Levina, L., Lu, Z. H. & Sargent, E. H. Efficient infrared electroluminescent devices using solution-processed colloidal quantum dots. *Adv. Funct. Mater.* **15**, 1865–1869 (2005).

86. Choudhury, K. R., Song, D. W. & Franky, S. Efficient solution-processed hybrid polymer–nanocrystal near infrared light-emitting devices. *Org. Electron.* **11**, 23–28 (2010).

730 87. Bourdakos, K. N., Dissanayake, D. M. N. M., Lutz, T., Silva, S. R. P. & Curry, R. J. Highly
731 efficient near-infrared hybrid organic-inorganic nanocrystal electroluminescence device. *Appl. Phys.*
732 *Lett.* **92**, 153311 (2008).
733 88. Sun, L. et al. Bright infrared quantum-dot light-emitting diodes through inter-dot spacing control.
734 *Nat. Nanotechnol.* **7**, 369–373 (2012).
735 89. Cheng, K.-Y., Anthony, R., Kortshagen, U. R. & Holmes, R. J. High efficiency silicon nanocrystal
736 light-emitting devices. *Nano Lett.* **11**, 1952–1956 (2011).
737 90. Franke, D. et al. Continuous injection synthesis of indium arsenide quantum dots emissive in the
738 short-wavelength infrared. *Nat. Commun* **7**, 12749 (2016).
739 91. Wijaya, H. et al. Efficient near-infrared light-emitting diodes based on In(Zn)As–In(Zn)P–GaP–
740 ZnS quantum dots. *Adv. Funct. Mater.* **30**, 1906483 (2020).
741 92. Chen, S. et al. InAs/GaAs quantum-dot superluminescent light-emitting diode monolithically
742 grown on a Si substrate. *ACS Photonics* **1**, 7, 638–642 (2014).
743 93. Hu, W. et al. Near-infrared quantum dot light emitting diodes employing electron transport
744 nanocrystals in a layered architecture. *Nanotechnology* **23**, 375202 (2012).
745 94. Ma, X., Xu, F., Benavides, J. & Cloutier, S. G. High performance hybrid near-infrared LEDs using
746 benzenedithiol cross-linked PbS colloidal nanocrystals. *Org. Electron.* **13**, 525–531 (2012).
747 95. Zhitomirsky, D., Voznyy, O., Hoogland, S. & Sargent, E. H. Measuring charge carrier diffusion in
748 coupled colloidal quantum dot solids. *ACS Nano* **7**, 5282–5290 (2013).
749 96. Sanchez, R. S. et al. All solution processed low turn-on voltage near infrared LEDs based on core–shell
750 PbS–CdS quantum dots with inverted device structure. *Nanoscale* **6**, 8551–8555 (2014).
751 97. Supran, G. J., et al. High-performance shortwave-infrared light-emitting devices using core–shell
752 (PbS–CdS) colloidal quantum dots. *Adv. Mater.* **27**, 1437–1442 (2015).

753 98. Yang, X. et al. Iodide capped PbS/CdS core-shell quantum dots for efficient long-wavelength
754 near-infrared light-emitting diodes. *Sci. Rep.* **7**, 14741 (2017).
755 99. Gong, X. et al. Highly efficient quantum dot near-infrared light-emitting diodes. *Nat. Photonics*
756 **10**, 253–257 (2016).
757 100. Ning, Z. et al. Quantum-dot-in-perovskite solids. *Nature* **523**, 324–328 (2015).
758 101. Gao, L. et al. Efficient near-infrared light-emitting diodes based on quantum dots in layered
759 perovskite. *Nat. Photonics* **14,** 227–233 (2020).
760 102. Vasilopoulou, M. *et al.* Efficient colloidal quantum dot light-emitting diodes operating in the
761 second near-infrared biological window. *Nat. Photonics* **14**, 50–56, (2020).
762 103. Pradhan, S. et al. High-efficiency colloidal quantum dot infrared light-emitting diodes via
763 engineering at the supra-nanocrystalline level. *Nat. Nanotechnol.* **14**, 72–79 (2019).
764 104. Pradhan, S., Dalmases, M., Baspinar, A.-B. & Konstantatos, G. Highly efficient, bright, and stable
765 colloidal quantum dot short-wave infrared light-emitting diodes. *Adv. Funct. Mater.* 2004445 (2020).
766 105. Li, L. et al. Self□filtered narrowband perovskite photodetectors with ultrafast and tuned spectral
767 response. *Adv. Optical Mater*. **5**, 1700672 (2017).
768 106. Dortaj, S. et al. High-speed and high-precision PbSe/PbI_2 solution process mid-infrared
769 camera. *Sci Rep* **11,** 1533 (2021).
770 107. Ullbrich, S. et al. Fast organic near-infrared photodetectors based on charge-transfer absorption. *J.*
771 *Phys. Chem. Lett.* **8**, 22, 5621–5625 (2017).
772 108. Shen, L. et al. Integration of perovskite and polymer photoactive layers to produce ultrafast
773 response, ultraviolet-to-near-infrared, sensitive photodetectors. *Mater. Horiz.* **4**, 242-248 (2017).
774 109. Gao, J., Nguyen, S., Bronstein, N. D. & Alivisatos, A. P. Solution-processed, high speed and high
775 quantum efficiency quantum dot infrared photodetectors. *ACS Photonics* **3**, 7, 1217–1222 (2016).

110. Quan, L. N. et al. Perovskites for next-generation optical sources. *Chem. Rev.* **119**, 12, 7444–7477 (2019).

111. Zhang, Q. et al. Light out-coupling management in perovskite LEDs-what can we learn from the past? *Adv. Funct. Mater.* **30**, 2002570 (2020).

112. Zhang, X., Hägglund , C. & Johansson, E. M. J. Electro-optics of colloidal quantum dot solids for thin-film solar cells. *Adv. Funct. Mater*. **26**, 1253-1260 (2016).

113. Xiao, Z. et al. Efficient perovskite light-emitting diodes featuring nanometre-sized crystallites. *Nat. Photonics* **11,** 108–115 (2017).

114. Miao, Y. et al. Microcavity top-emission perovskite light-emitting diodes. *Light Sci. Appl.* **9,** 89 (2020).

115. Shen, Y. et al. High□efficiency perovskite light□emitting diodes with synergetic outcoupling enhancement. *Adv. Mater.* **31**, 1901517 (2019).

116. Zhao, L., Lee, K. M., Roh, K., Khan, S. U. Z. & Rand, B.P. Improved outcoupling efficiency and stability of perovskite light□emitting diodes using thin emitting layers. *Adv. Mater.* **31**, 1805836 (2019).

117. Cho, C. et al. The role of photon recycling in perovskite light-emitting diodes. *Nat. Commun*. **11**, 611 (2020).

118. Murawski, C., Leo, K. & Gather, M. C. Efficiency roll-off in organic light-emitting diodes. *Adv. Mater.* **25**, 6801–6827 (2013).

119. Sassi, M. *et al.* Near-infrared roll-off-free electroluminescence from highly stable diketopyrrolopyrrole light emitting diodes. *Sci. Rep.* **6,** 34096 (2016).

120. Bencheikh, F., Sandanayaka, A. S. D., Fukunaga, T. Matsushima, T. & Adachi. C. Origin of external quantum efficiency roll-off in 4,4′-bis[(*N*-carbazole)styryl]biphenyl (BSBCz)-based inverted organic light emitting diode under high pulsed electrical excitation. *J. Appl. Physics* **126**, 185501 (2019).

121. Swayamprabha, S. S. et al. Approaches for long lifetime organic light emitting diodes. *Adv. Science* **8**, 2002254 (2020).

122. Matsushima, T. *et al.* High performance from extraordinarily thick organic light-emitting diodes. *Nature* **572,** 502–506 (2019).

123. Titov, A. *et al.* 6-3: Quantum dot LEDs: Problems & prospects. *SID Symp. Dig. Tech. Pap.* **48**, 58–60 (2017).

124. Gao, Y. et al. Disorder strongly enhances Auger recombination in conductive quantum-dot solids. *Nat. Commun.* **4,** 2329 (2013).

125. Kim, K. *et al.* Hybrid perovskite light emitting diodes under intense electrical excitation. *Nat. Commun.* **9**, 4893 (2018).

126. Fakharuddin, A. *et al.* Reduced efficiency roll-off and improved stability of mixed 2D/3D perovskite light emitting diodes by balancing charge injection. *Adv. Funct. Mater.* **29**, 1904101 (2019).

127. Zhao, X. & Tan, Z.-K. Large-area near-infrared perovskite light-emitting diodes. *Nat. Photonics* **14**, 215–218 (2020).

128. Zhao, L. et al. Thermal management enables bright and stable perovskite light□emitting diodes. *Adv. Mater.* **32**, 2000752 (2020).

129. Zou, C., Liu, Y., Ginger, D. S. & Lin, L. Y. Suppressing efficiency roll-off at high current densities for ultra-bright green perovskite light-emitting diodes. *ACS Nano* **14**, 5, 6076–6086 (2020).

130. Yoshida, K., Nakanotani, H. & Adachi, C. Effect of Joule heating on transient current and electroluminescence in p-i-n organic light-emitting diodes under pulsed voltage operation. *Org. Electron.* **31**, 287–294 (2016).

131. Kim, H. et al. Proton-transfer-induced 3D/2D hybrid perovskites suppress ion migration and reduce luminance overshoot. *Nat. Commun.* **11,** 3378 (2020).

132. Prakasam, V, Tordera, D., Bolink, H. J. & Gelinck, G. Degradation mechanisms in organic lead halide perovskite light□emitting diodes. *Adv. Optical Mater.* 7, 1900902 (2020).

133. Guo, Y. *et al.* Phenylalkylammonium passivation enables perovskite light emitting diodes with record high-radiance operational lifetime: the chain length matters. *Nat. Commun.* **12,** 644 (2021).

134. Yuan, Z. et al. Unveiling the synergistic effect of precursor stoichiometry and interfacial reactions for perovskite light-emitting diodes. *Nat. Commun.* **10,** 2818 (2019).

135. Moroz, P. et al. Infrared emitting PbS nanocrystal solids through matrix encapsulation. *Chem. Mater.* **26**, 14, 4256–4264 (2014).

136. Xie, C., Zhao, X., Ong, E. W. Y. & Tan, Z.-K. Transparent near-infrared perovskite light-emitting diodes. *Nat. Commun*. **11**, 4213 (2020).

Acknowledgements

M.V. acknowledges funding by the project "Development of Materials and Devices for Industrial, Health, Environmental and Cultural Applications" (MIS 5002567), which is implemented under the "Action for the Strategic Development on the Research and Technological Sector", funded by the Operational Programme "Competitiveness, Entrepreneurship and Innovation" (NSRF 2014-2020) and co-financed by Greece and the European Union (European Regional Development Fund). H.J.B. acknowledges funding from the European Research Council (ERC) under the European Union's Horizon 2020 research and innovation programme (grant agreement no. 834431) and the Spanish Ministry of Science, Innovation and Universities MAT2017-88821-R and CEX2019-000919-M. F.P.G.d.A. and E.H.S. acknowledge support from the Canada Research Chair.

Competing interests

The authors declare no competing interests.

Additional information

Correspondence should be addressed to M.V., H. J. B. or E. H. S.

Supplementary Information

Tables including key figure of merits and stability data of solution-processed NIR LEDs,

Box 1

The device architecture and key performance parameters of solution-processed NIR-LEDs

Typical solution-processed NIR-LEDs consist of a multilayer architecture, embedding the semiconductor emissive layer (EML) between an electron-injection (EIL) and a hole-injection layer (HIL), similarly to their visible emitting counterparts, as illustrated in the Scheme 1a. In some cases, appropriate interlayers are also applied to block opposite charges from leaking through the device (which are the hole blocking layer, HBL, and the electron blocking layer, EBL). Under forward bias, electrons and holes injected from the electrodes drift and diffuse within the EML (electrons are transferred to the lowest occupied molecular orbital, LUMO, of the organic emissive semiconductor or the conduction band minimum of the inorganic ones, such as perovskites and colloidal quantum dots, whereas holes are transferred towards the highest occupied molecular orbital, HOMO, or the valence band maximum of either the organic or the inorganic semiconductor, respectively, see Scheme 1b), and eventually recombine emitting photons or heat.

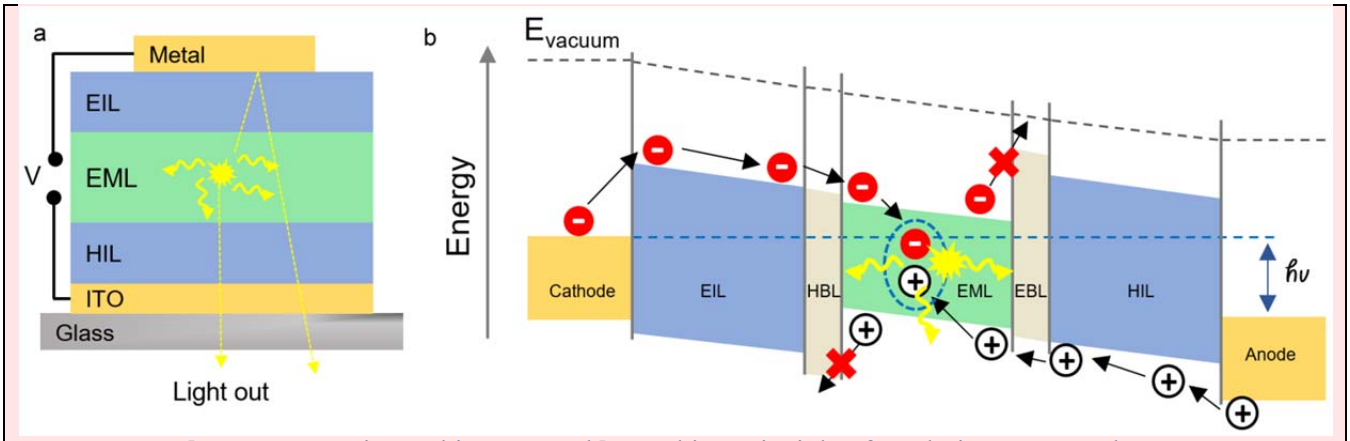

Scheme 1 a, Device architecture and **b**, working principle of a solution-processed LED.

The key performance parameters of a NIR-LED are the the external quantum efficiency (EQE), the power density (P) or radiance, the device lifetime and efficiency roll-off. EQE denotes the ratio of emitted photons versus the injected charges under external bias and is expressed as the product of the internal quantum efficiency (IQE) and the light outcoupling efficiency (η_{out}) (Eq. 1):

$$EQE = \frac{emitted\ photons}{injected\ charges} = IQE \times \eta_{out} \qquad (1)$$

The η_{out} is the outcoupling efficiency while the IQE value (Eq. 2) is proportional to the probability for radiative decay to occur (r), the photoluminescence quantum yield of the emitter (PLQY or φ_{PL}), and to the probability that electrons and holes recombining (γ):

$$IQE = r \times \varphi_{PL} \times \gamma \qquad (2)$$

Luminance is a figure of merit not relevant to NIR-LEDs thus measuring the amount of radiant intensity per unit projected area (the so-called radiance given in W m^{-2} sr^{-1}) is more appropriate.

The emitted light intensity or power output density (P) of an NIR-LED is important for applications, such as spectroscopy and sensing. This, is proportional to the EQE and the current density (J) (Eq. 3):

$$P = \frac{E_\nu J}{q} EQE \qquad (3)$$

where EQE is derived by Eq. 1, E_ν is the energy of a photon and q is the elementary charge.

Figure captions

Fig. 1 Applicability and scalability of solution-processed NIR-LEDs. a, The infrared spectral region and illustration of selected applications. NIR, near-infrared; SWIR, short-wave infrared. MIR, mid-infrared; NIR sources are in demand for application in biosensing, optogenetics, biometrics, night vision, data storage, surveillance and 3D imaging. Biological transparency windows are defined as follows: first (NIR-I, 650-950 nm), second (NIR□II, 1100–1350 nm), third (NIR-III, 1600–1870 nm) and fourth (NIR-IV, centred at 2200 nm) NIR windows that allow for clearer imaging due to a scattering and absorption reduction. The telecom window between 800–900 nm was originally used for transmitting information, followed by the range 1260–1360 nm (or O-band) for short distance communication, while today the 1530–1565 nm range (known as the C-band) is the most commonly

used band for long haul optical transmission. **b**, Solution-processed NIR-LEDs can be processed from inks using various methods as shown.

Fig. 2 NIR emission from organic semiconductors. Energy diagram depicting photophysical processes for light emission: **a**, fluorescence (1), phosphorescence (2), intersystem crossing (ISC) from singlet to triplet levels, and thermally activated delayed fluorescence (3), obtained upon reverse intersystem crossing (RISC). **b**, Delayed fluorescence (DF) (4) due to triplet-triplet annihilation (TTA). **c**, Singlet fission to two triplets (5). **d**, Molecular parameters controlling bandgap narrowing in organic chromophores. **e**, Photoluminescence quantum yield (φ_{PL}) for different organic chromophores in relation to their emission wavelength. The dashed line is guide to the eye. **f**, Electroluminescence by selective HOMO and SOMO hole and electron injection. The scheme shows two routes to create D_1 (first doublet excited state. $[S]^-$ and $[S, T_0, T_+, T_-]^+$ denote negatively and positively charged intermediates. **g**, PLQY values of CBP blend films doped with the curcuminoid NIR TADF emitter (shown as inset) at various concentrations. **h**, Chemical structures of Pt(II) phosphorescence complexes 1–3: $[Pt(fprpz)_2]$ (compound 1), Pt(fprpz)(fppz)] (compound 2), [Pt(fprpz)(tbfppz)] (compound 3) and **i**, their normalized PL spectra in thin films. Panels reproduced with permission from: **d**, ref.[11] Wiley-VCH; **e**, ref.[22] Wiley-VCH; **f**, ref.[28], Springer Nature Ltd; **g,** ref.[32], Springer Nature Ltd; **h,i,** ref.[46], Springer Nature Ltd.

Fig. 3 NIR light emission from perovskite LEDs. a, Illustration of the crystal structure of dimensionally engineered halide pure-phase (n = 1, 2 & 3), mixed phase (2D/3D) and a classical polycrystalline 3D perovskite. **b,** Schematic showing energy (charge) funneling from larger to smaller bandgap perovskite domains. The process takes place at ultrafast timescale (ps). **c,** Formation of submicrometre perovskite structure via solution processing. **d,** Photoluminescence (PL) and electroluminescence (EL) spectra of the device at different viewing angles. **e-g,** Device architecture, EL spectra and EQE curves of LEDs employing 3D perovskite nanocrystals embedded in an electron-transport molecular matrix of 4,4′-diaminodiphenyl sulfone (DDS). Panels reproduced with permission from: **c,d**, ref.[58] Wiley-VCH; **e-g** ref.[60], Springer Nature Ltd.

Fig. 4 NIR emission from colloidal QDs. a, Normalized photoluminescence from QDs with a core-shell structure (shown as inset). **b,** QD-in-perovskite approach: radiative recombination dominates when QDs and perovskite are lattice matched (left). Lattice mismatch causes interfacial defects (dash line) and non-radiative recombination (right). **c**, Variation of EQE with J in devices using mixed halide perovskite matrices with different iodine molar concentrations. **d**, The emitter only QD array approach: The pink spheres are the emissive QDs and purple spheres represent defective QDs. The charge-collection zones illustrated as yellow circles around the QDs are defined by the carrier diffusion length (L_d). **e**, The matrix inclusion architecture: large QD are dispersed in a matrix of smaller QDs. Radiative recombination channels (green circles) increase whereas non-radiative recombination channels decrease. **f,** EQE of the single, binary and ternary devices plotted against injected current. Panels reproduced with

permission from: **a**, ref.[75], Springer Nature Ltd; **b**,**c**, ref.[99], Springer Nature Ltd; **d**,**e**,**f**. ref.[103], Springer Nature Ltd.

Fig. 5 Figure of merits of NIR-LEDs. a, EQE-wavelength of solution-processed NIR-LEDs based on results of Supplementary Table 1. **b**, EQE roll-off of state-of-the-art TADF[32] and phosphorescence[40] OLED, QDLED[103], hybrid (QD-in-perovskite) QDLED[101], 3D[61] and 2D[65] PeLEDs and 3D μ-PeLED[128] as a function of current density. **c**,**d**, Reported lifetime of various solution-processed NIR-LEDs based on the data provided in Supplementary Table 2. In Fig. 5c the lifetime is plotted versus the initial device radiance (given in W sr^{-1} m^{-2}) except for the OLED device where the initial irradiance is presented. In Fig. 5d the lifetime is plotted versus injected current density into the device. T_{85} and T_{50} (or half-lifetime) denote the time of constant operation until the light output decreases to 85% and 50%, respectively, of the initial value.

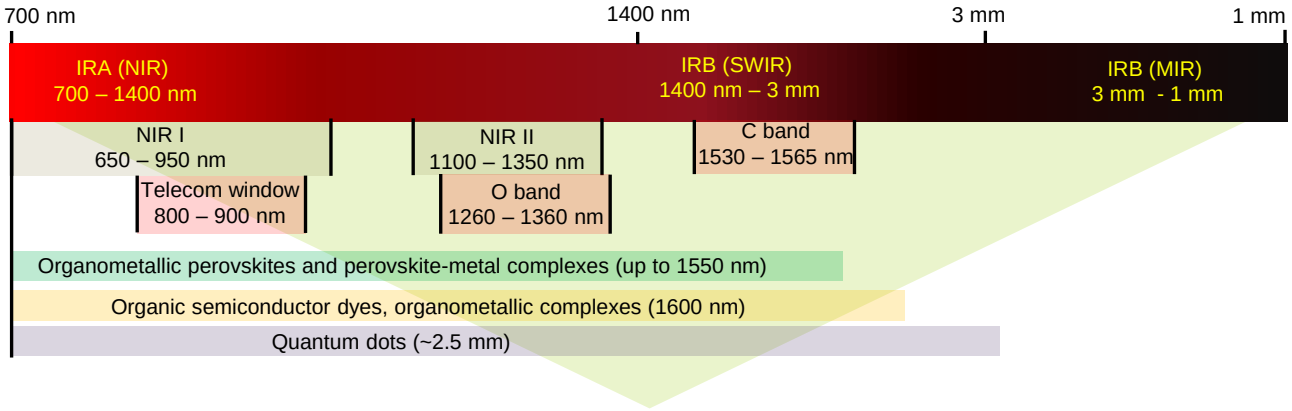
700 nm
1400 nm
3 mm
1 mm
IRA (NIR)
700 – 1400 nm
IRB (SWIR)
1400 nm – 3 mm
IRB (MIR)
3 mm - 1 mm
NIR I
650 – 950 nm
Telecom window
800 – 900 nm
NIR II
1100 – 1350 nm
O band
1260 – 1360 nm
C band
1530 – 1565 nm
Organometallic perovskites and perovskite-metal complexes (up to 1550 nm)
Organic semiconductor dyes, organometallic complexes (1600 nm)
Quantum dots (~2.5 mm)

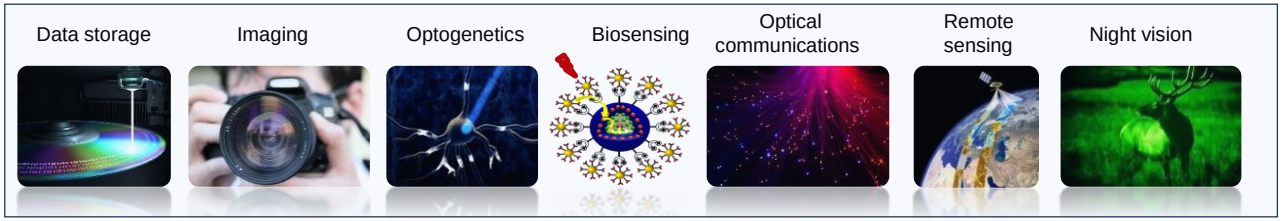
Data storage
Imaging
Optogenetics
Biosensing
Optical communications
Remote sensing
Night vision

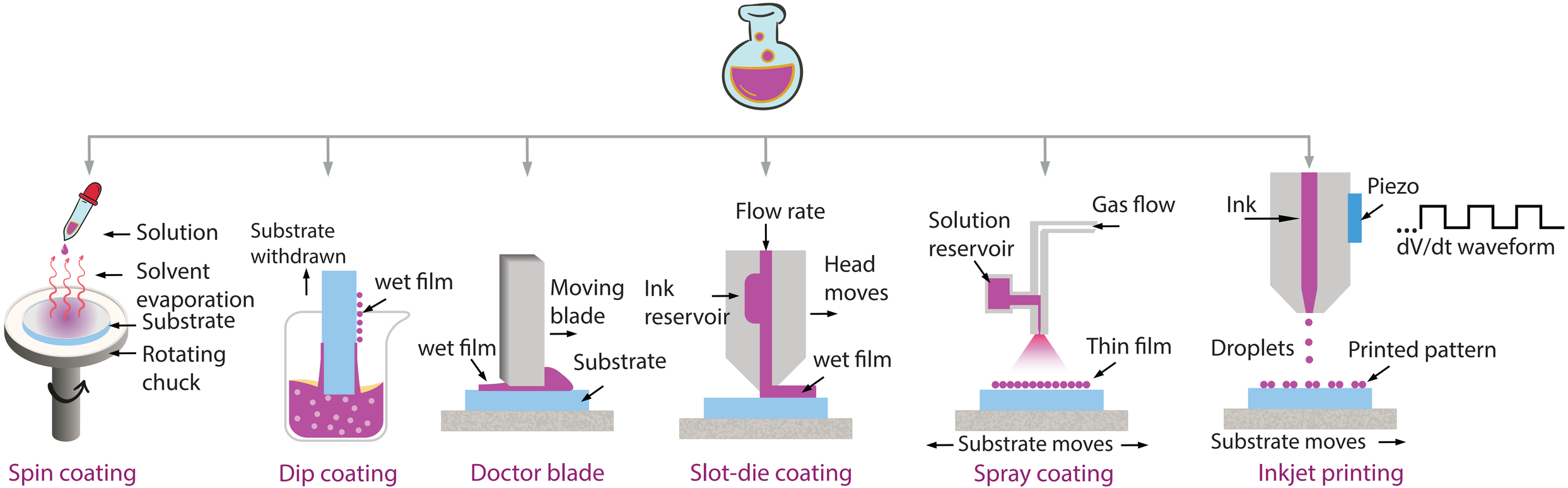
Solution
Solvent evaporation
Substrate
Rotating chuck
Spin coating
Substrate withdrawn
wet film
Dip coating
Moving blade
wet film
Substrate
Doctor blade
Flow rate
Ink reservoir
Head moves
wet film
Slot-die coating
Solution reservoir
Gas flow
Thin film
Substrate moves
Spray coating
Ink
Piezo
dV/dt waveform
Droplets
Printed pattern
Substrate moves
Inkjet printing

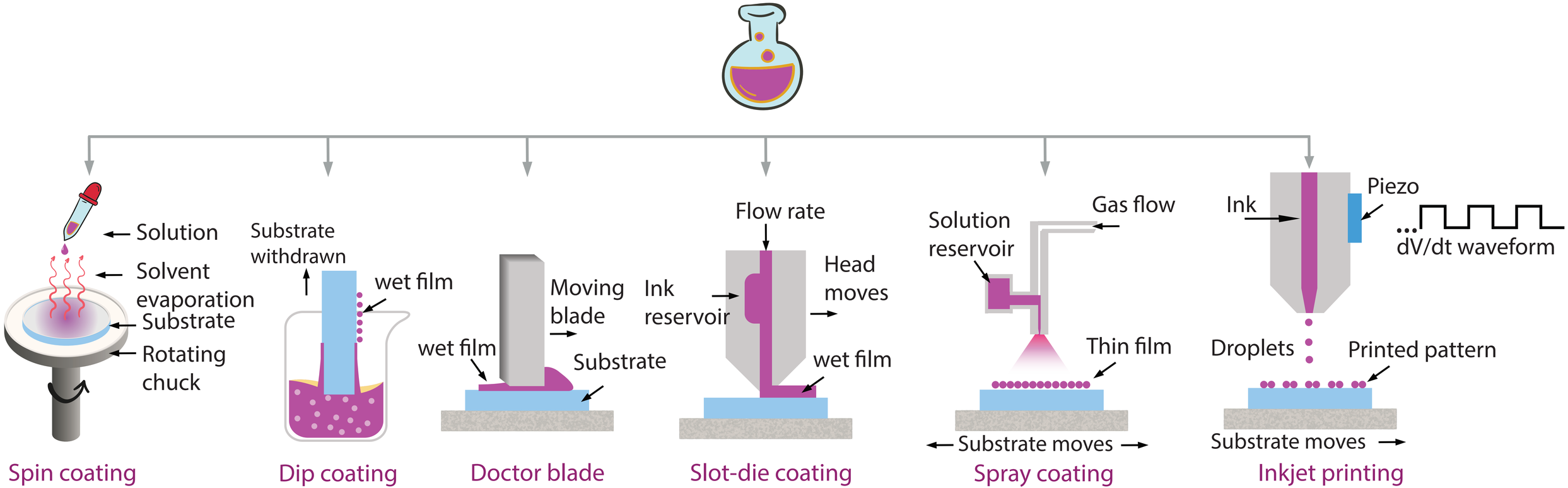
Solution
Solvent evaporation
Substrate
Rotating chuck
Spin coating
Substrate withdrawn
wet film
Dip coating
Moving blade
wet film
Substrate
Doctor blade
Flow rate
Ink reservoir
Head moves
wet film
Slot-die coating
Solution reservoir
Gas flow
Thin film
Substrate moves
Spray coating
Ink
Piezo
dV/dt waveform
Droplets
Printed pattern
Substrate moves
Inkjet printing

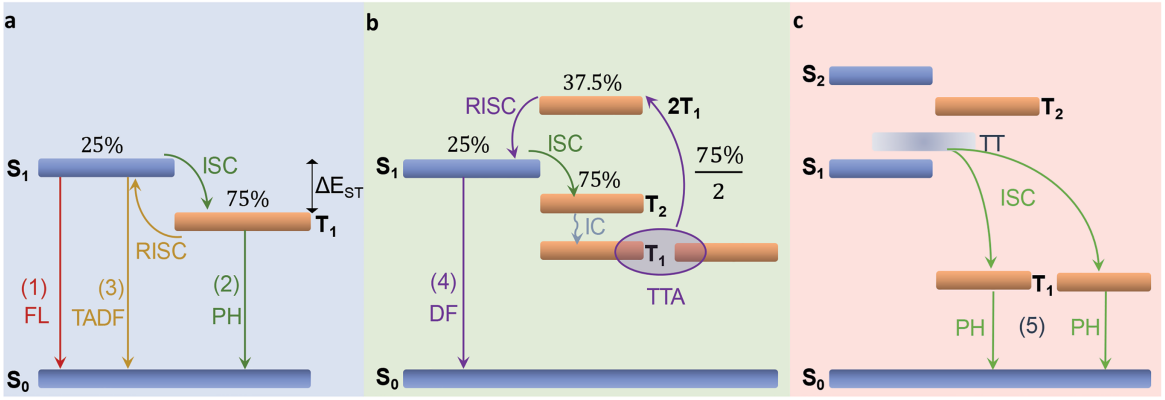
a
25%
S1
ISC
75%
ΔEST
T1
RISC
(1)
FL
(3)
TADF
(2)
PH
S0
b
37.5%
RISC
2T1
25%
ISC
75%
S1
75%
2
T2
IC
T1
(4)
DF
TTA
S0
c
S2
T2
TT
S1
ISC
T1
PH
(5)
PH
S0

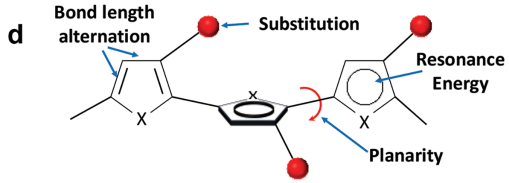
d
Bond length alternation
Substitution
Resonance Energy
Planarity
X

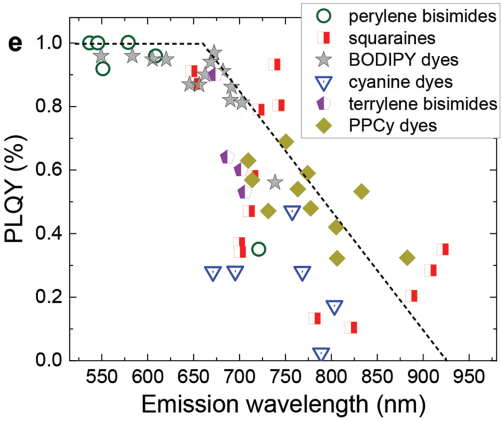
e
perylene bisimides
squaraines
BODIPY dyes
cyanine dyes
terrylene bisimides
PPCy dyes
PLQY (%)
Emission wavelength (nm)

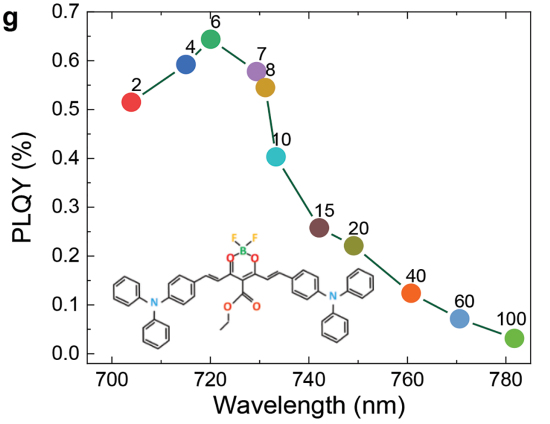
g
PLQY (%)
Wavelength (nm)
2
4
6
7
8
10
15
20
40
60
100

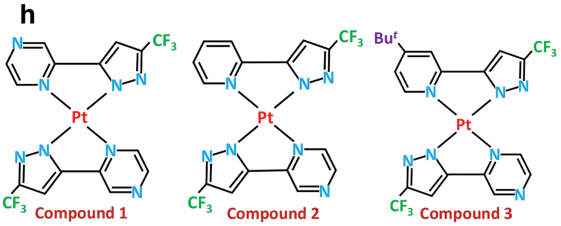
h
Compound 1
Compound 2
Compound 3

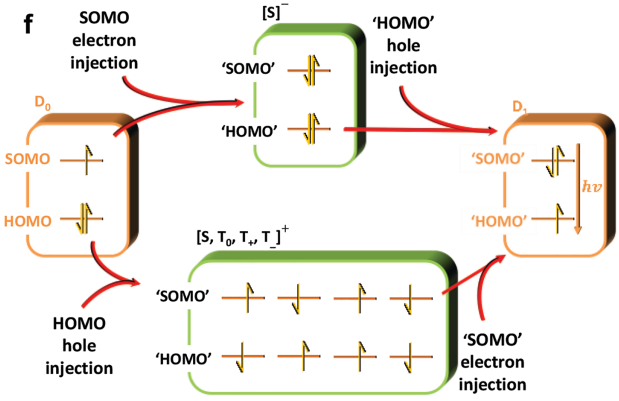
f
SOMO electron injection
[S]−
'SOMO'
'HOMO'
'HOMO' hole injection
D0
SOMO
HOMO
D1
'SOMO'
'HOMO'
hν
[S, T0, T+, T−]+
'SOMO'
'HOMO'
HOMO hole injection
'SOMO' electron injection

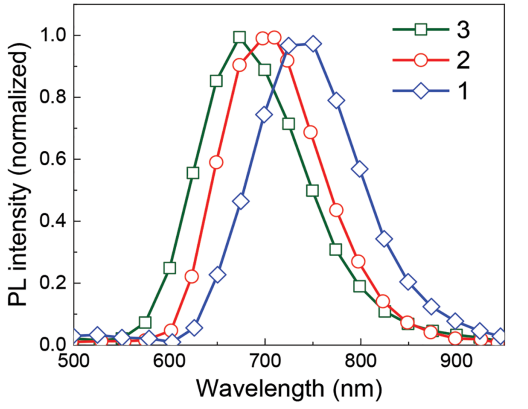
i
PL intensity (normalized)
Wavelength (nm)
3
2
1

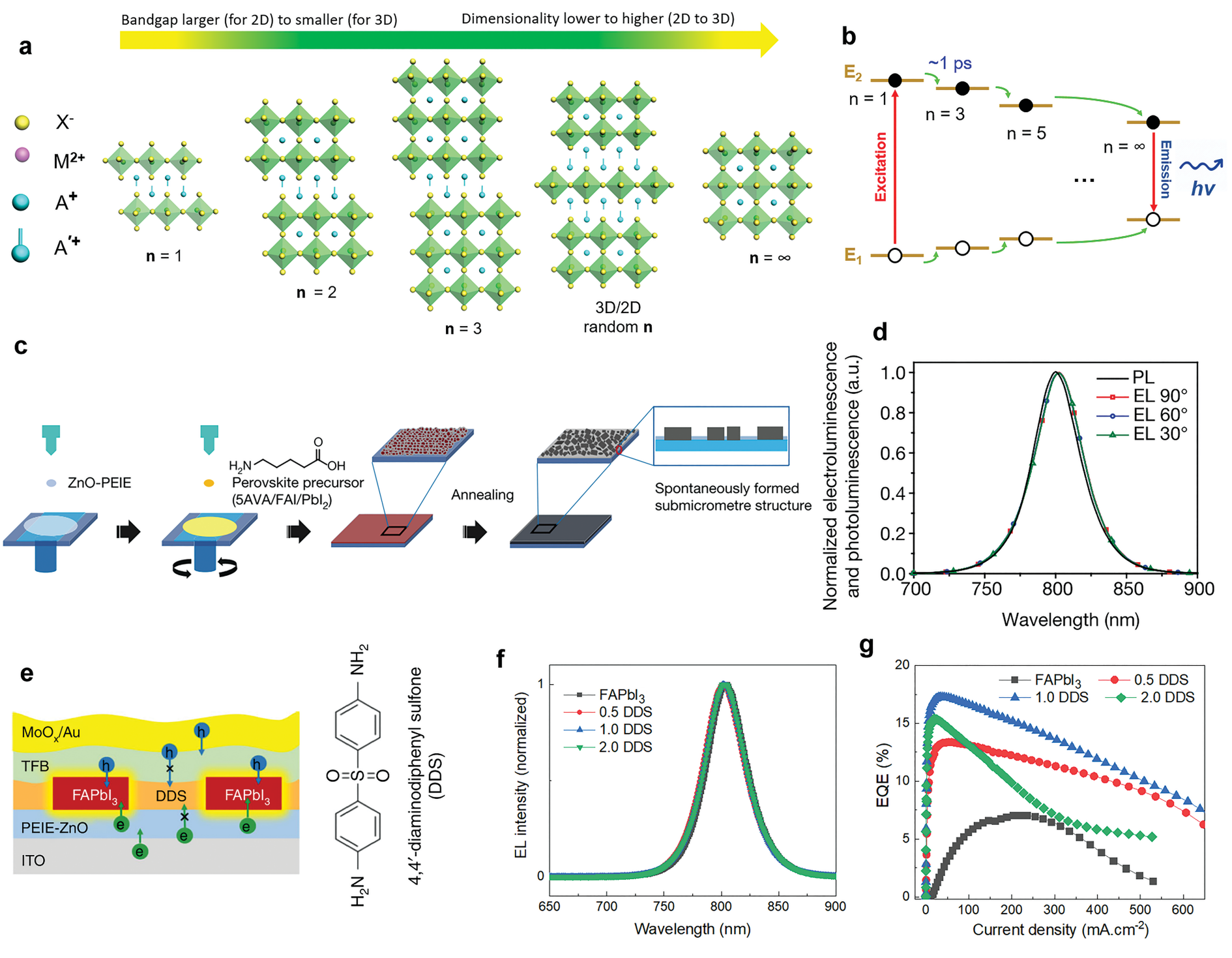
a
Bandgap larger (for 2D) to smaller (for 3D)
Dimensionality lower to higher (2D to 3D)
X-
M2+
A+
A'+
n = 1
n = 2
n = 3
3D/2D
random n
n = ∞
b
E2
n = 1
~1 ps
n = 3
n = 5
n = ∞
Excitation
Emission
hv
E1
c
ZnO-PEIE
Perovskite precursor
(5AVA/FAI/PbI2)
Annealing
Spontaneously formed
submicrometre structure
d
Normalized electroluminescence
and photoluminescence (a.u.)
PL
EL 90°
EL 60°
EL 30°
Wavelength (nm)
e
MoOx/Au
TFB
FAPbI3
DDS
FAPbI3
PEIE-ZnO
ITO
4,4'-diaminodiphenyl sulfone
(DDS)
f
EL intensity (normalized)
FAPbI3
0.5 DDS
1.0 DDS
2.0 DDS
Wavelength (nm)
g
EQE (%)
FAPbI3
0.5 DDS
1.0 DDS
2.0 DDS
Current density (mA.cm-2)

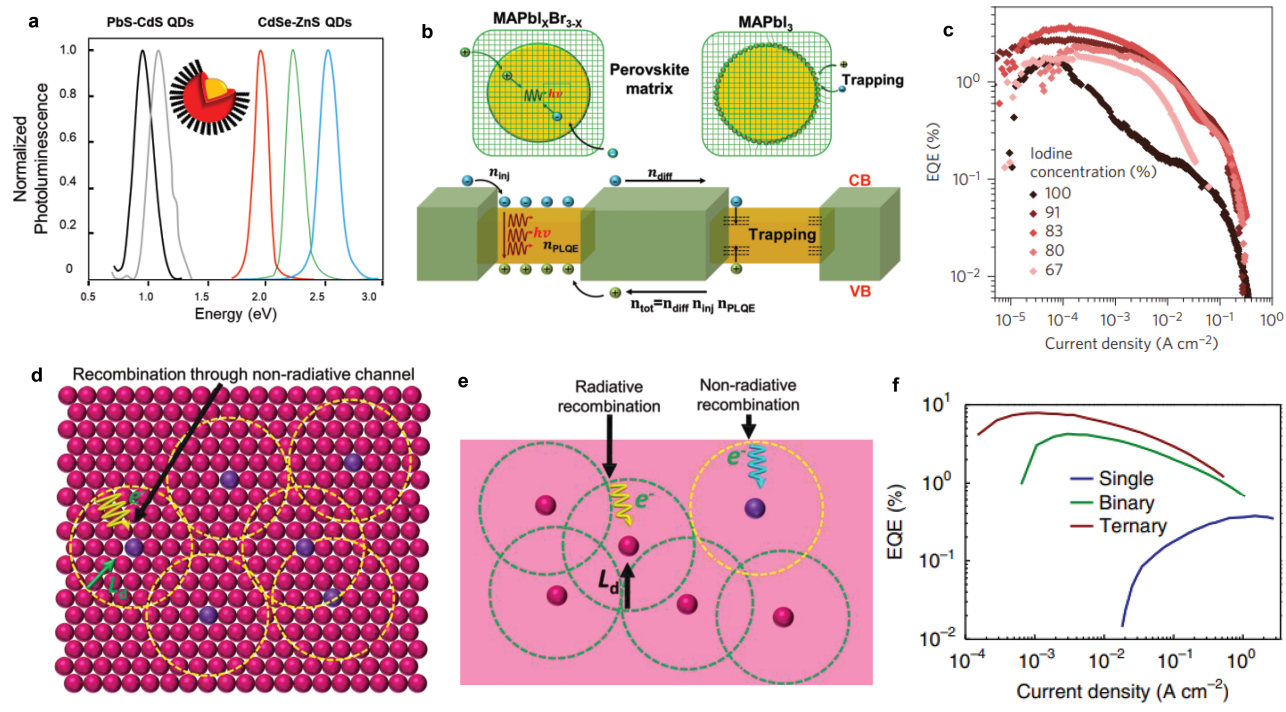
a
PbS-CdS QDs
CdSe-ZnS QDs
Normalized Photoluminescence
Energy (eV)
b
MAPbI3-xBrx
MAPbI3
Perovskite matrix
Trapping
CB
VB
ninj
ndiff
nPLQE
Trapping
ntot=ndiff ninj nPLQE
c
EQE (%)
Iodine concentration (%)
100
91
83
80
67
Current density (A cm−2)
d
Recombination through non-radiative channel
e
Radiative recombination
Non-radiative recombination
Ld
f
EQE (%)
Single
Binary
Ternary
Current density (A cm−2)

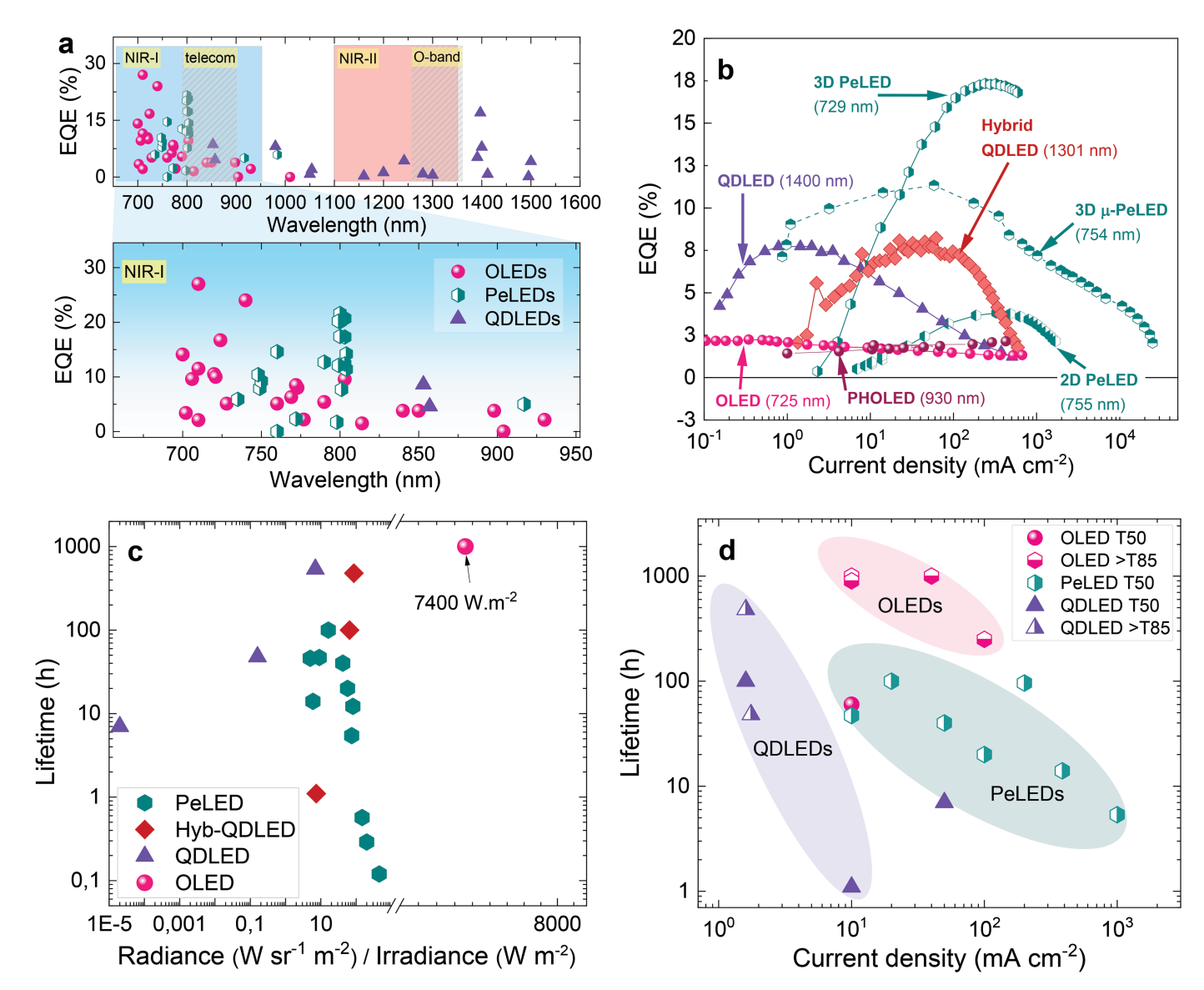
a
NIR-I
telecom
NIR-II
O-band
EQE (%)
Wavelength (nm)
OLEDs
PeLEDs
QDLEDs
b
3D PeLED
(729 nm)
Hybrid
QDLED (1301 nm)
QDLED (1400 nm)
3D μ-PeLED
(754 nm)
OLED (725 nm)
PHOLED (930 nm)
2D PeLED
(755 nm)
Current density (mA cm-2)
c
7400 W.m-2
PeLED
Hyb-QDLED
QDLED
OLED
Lifetime (h)
Radiance (W sr-1 m-2) / Irradiance (W m-2)
d
OLED T50
OLED >T85
PeLED T50
QDLED T50
QDLED >T85
OLEDs
QDLEDs
PeLEDs
Lifetime (h)
Current density (mA cm-2)

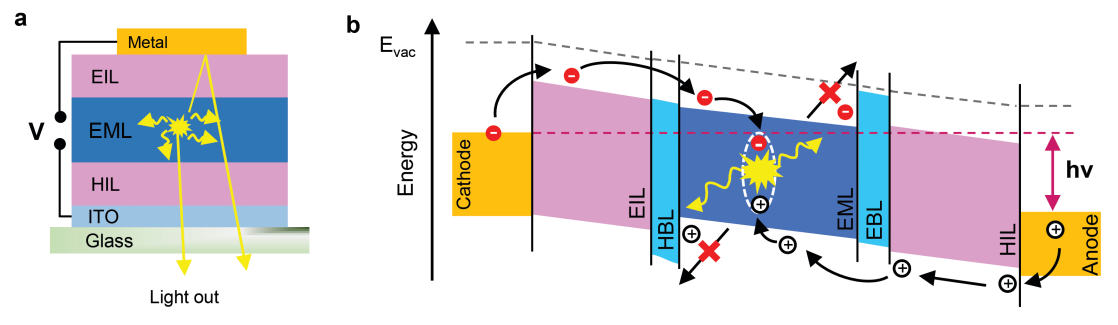
a
Metal
EIL
EML
V
HIL
ITO
Glass
Light out
b
E vac
Energy
Cathode
EIL
HBL
EML
EBL
HIL
hv
Anode